NOVA SCHOOL OF SCIENCE & TECHNOLOGY

DEPARTAMENT OF PHYSICS

CRISTINA ALEJANDRA PAUBLINI ORNELAS

Bachelor Degree in Biomedical Engineering Sciences

GRAPHENE BIOSENSORS FOR DIABETIC FOOT ULCER MONITORING

MASTER IN BIOMEDICAL ENGINEERING

NOVA University Lisbon

September, 2022

DEPARTAMENT OF PHYSICS

GRAPHENE BIOSENSORS FOR DIABETIC FOOT ULCER MONITORING

CRISTINA ALEJANDRA PAUBLINI ORNELAS

Bachelor Degree in Biomedical Engineering Sciences

Adviser: Dr. João Coelho
Researcher CENIMAT|I3n, NOVA School of Sciences and Technology (FCT-NOVA)

Co-advisers: Dr. Maria João Meneses
Postdoctoral Researcher, iNOVA4Health, NOVA Medical School (NMS)

Examination Committee:

Chair: Dr. Célia Henriques,
Associated Professor, NOVA School of Sciences and Technology (FCT-NOVA)

Rapporteurs: Dr. Joana Vaz Pinto,
Assistant Professor, NOVA School of Sciences and Technology (FCT-NOVA)

Adviser: Dr. João Coelho,
Researcher CENIMAT|I3n, NOVA School of Sciences and Technology (FCT-NOVA)

MASTER IN BIOMEDICAL ENGINEERING

NOVA University Lisbon
September, 2022

Dedicado aos meus pais e irmãs.

AGRADECIMENTOS

A elaboração desta dissertação de mestrado contou com muitos e importantes apoios, sem os quais esta etapa académica e pessoal não poderia ser alcançada. Sendo assim, quero expressar os meus sinceros agradecimentos a todas as pessoas e instituições que, direta ou indiretamente, contribuíram para a realização desta dissertação.

Em primeiro lugar, queria agradecer à Professora Elvira Fortunato, pela oportunidade de trabalhar neste centro de investigação de excelência, onde se reuniam as condições para desenvolvimento desta dissertação. Em seguida queria dar um especial agradecimento aos meus orientadores Dr. João Coelho e Dra. Maria João Meneses por me terem acompanhado durante este percurso, pela confiança, dedicação, por todos os conhecimentos científicos transmitido e pela boa disposição. Admiro muito o vosso trabalho, curiosidade e constante busca pela eficiência. Agradeço ao Ricardo Correia pela disponibilidade, sugestões e apoio ao longo desta dissertação. Também queria agradecer à Alexandra Gonçalves, Maria Morais, Tomás Pinheiro, Tiago Carvalho, Raquel Barras, Guilherme Ribeiro, e a toda a equipa do CENIMAT pela forma como me integraram, pela ajuda que me deram e por tornar o ambiente do laboratório agradável e risonho.

À Universidade Nova de Lisboa e ao Santander, pela atribuição do Prémio de Investigação Colaborativa Santander/NOVA 2021 e financiamento do projeto "Pensos Inteligentes de Grafeno para a Monitorização da Úlcera do Pé Diabético", ao abrigo do qual desenvolvi esta dissertação de mestrado.

Aos meus amigos do coração Mariana Pinto e Pedro Rodrigues, por todo o apoio e por todos os momentos fantásticos e por aqueles que estão por vir. As minhas amigas desde o primeiro dia da faculdade, Beatriz Mendonça, Liu Sofia e Ana Fonseca, por todas as conversas motivadoras, lanches na relva. À minha colega de laboratório e grande amiga Joana Jorge, obrigada pela entreajuda, desabafos e risadas à hora do almoço que tanto ajudaram a desanuviar.

Aos meus pais que sempre acreditaram no meu potencial, pelo vosso amor e pelos ensinamentos transmitidos que fazem a pessoa que hoje sou. À paciência e carinho das minhas irmãs, que de tanto me ouvir falar da tese são expertas no tema.

“There are always flowers for those who want to see them.” (Henri Matisse).

ABSTRACT

The prevalence of Diabetes Mellitus (DM) in the twenty-first century has increased drastically, consequently, the incidence of DM-related complications has increased as well. According to the International Diabetes Federation (IDF) in 2021, globally one in every ten adults aged from 20 to 79 years had DM. Approximately 15-34% of individuals with DM are likely to develop a Diabetic Foot Ulcer (DFU) throughout their lifetime. Unmonitored and infected DFU can lead to non-traumatic lower extremity amputation and worst-case cause morbidity. Therefore, it is of great importance to develop effective, rapid production, biocompatible, low-cost, flexible, wearable, sustainable sensors to monitor objectively the ulcer healing state. This dissertation aims to meet this need through the development of temperature and pH laser-induced graphene (LIG) sensors on paper, that could be included in smart bandages and medical wound dressings. During this dissertation, LIG on paper fabrication parameters were studied to obtain the most reproducible, durable, and good electrical performance. The production condition of the LIG used for the development of the sensors had an average sheet resistance value of $24.9\Omega/sq$ with $1.2\ \Omega/sq$ of standard deviation. The thermoresistive sensor developed is characterized by a negative temperature coefficient with a highly linear response, and a sensitivity of $0.71\ \%℃^{-1}$ from 26℃ to 40℃, a suitable interval for its application. The electrochemical cell produced works as a potentiometric pH sensor. Its working electrode (WE) was electropolymerized with polyaniline (PANI) a pH-sensitive biocompatible electrolyte. The sensor demonstrated a *Nernstian* behavior with a sensitivity of $53.0\ mV/pH$ and $2.3\ mV/pH$ of standard deviation on the interval from 2 pH to 9 pH.

Keywords: laser induced graphene, paper biosensor, thermoresistive, pH, diabetic foot ulcer, polyaniline

RESUMO

A prevalência da Diabetes Mellitus (DM) no século XXI aumentou drasticamente, consequentemente, a incidência de complicações relacionadas com a DM também aumentou. Segundo a Federação Internacional de Diabetes em 2021, globalmente um em cada dez adultos com idades compreendidas entre os 20 e os 79 anos tem DM. Aproximadamente 15-34% dos indivíduos com DM são suscetíveis de desenvolver uma úlcera do pé diabético (DFU) durante toda a sua vida. A DFU não monitorizada e infetada pode levar a uma amputação não traumática das extremidades inferiores e causar morbilidade no pior dos casos. Por conseguinte, é de grande importância desenvolver sensores eficazes, de produção rápida, biocompatíveis, de baixo custo, flexíveis, viáveis e sustentáveis para monitorizar objetivamente o estado de cicatrização da úlcera. Esta tese visa responder a esta necessidade através do desenvolvimento de sensores de temperatura e pH induzidos por laser (LIG) em papel, que poderiam ser incluídos em ligaduras inteligentes e curativos médicos de feridas. Durante esta dissertação, foram estudados parâmetros de fabrico de LIG em papel para obter o mais reprodutível, durável, e bom desempenho elétrico. O valor da resistência da folha média da condição de produção utilizada para o desenvolvimento foi de $24.9\ \Omega/sq$ com um desvio padrão de $1.2\ \Omega/sq$. O sensor termoresistivo desenvolvido é caracterizado por um coeficiente de temperatura negativa com uma resposta altamente linear, e uma sensibilidade de $0.71\ \%℃^{-1}$ entre os $26℃$ e $40℃$, um intervalo adequado para a sua aplicação. A célula eletroquímica produzida funciona como um sensor de pH potenciométrico. O seu elétrodo de trabalho (WE) foi electropolimerizado com polianilina (PANI) um eletrólito biocompatível sensível ao pH. O sensor demonstrou um comportamento *Nernstiano* com uma sensibilidade de $53.0\ mV/pH$ e desvio padrão de $2.3 mV/pH$ no intervalo de 2 a 9 pH.

Palavras-chave: grafeno induzido por laser, biossensor de papel, termoresistivo, pH, úlcera do pé diabético, polianilina

CONTENTS

LIST OF FIGURES

List of Tables

ABBREVIATIONS

BR	Britton Robbinson Buffer Solution
CE	Couter Electrode
CV	Cyclic Voltammetry
DFU	Diabetic Foot Ulcer
DM	Diabetes Mellitus
EDS	Energy-Dispersive X-ray Spectroscopy
IGF-1	Insulin Like Growth Factor - 1
IL-1β	Interleukin-1 beta
LIG	Laser Induced Graphene
NTC	Negative Temperature Coefficient
OCP	Open Circuit Potentiometry
PANI	Polyaniline
PDMS	Polydimethylsiloxane
PI	Polyimide
PPI	Pulses Per Inch
PTC	Positive Temperature Coefficient
RE	Reference Electrode
RSV	Relative Standard Deviation
RTD	Resistive Temperature Detector
SEM	Scanning Electron Microscopy
TCR	Temperature coefficient resistance

TGFβ	Transforming Factor - β
TNFα	Tumor necrosis factor
WE	Working Electrode

1. INTRODUCTION

This introductory chapter aims to present insight and contextualize the reader, but also calling its attention to the significance of the conducted study. Additionally, in this chapter a brief presentation of the dissertation purpose and organization is made.

1.1. Context and Motivation

Diabetes Mellitus (DM) refers to a group of metabolic disorders that share the phenotype of hyperglycemia due to deficiency of insulin secretion, insulin resistance, or both [1], [2]. Nowadays, DM affects globally 10% of adults between 20 to 79 years [3].

Diabetic foot ulcer (DFU) consist on the most rapid aggravating chronic complication associated with DM progression [4][5]. DM patients are prone to develop chronic, non-healing wounds that can lead to destruction of deeper tissues and infections from initially harmless injuries as a result of abnormal peripheral healing caused by the pathophysiology of DM [2], [5], [6]. It is estimated that around 15% to 25% of DM patients will develop DFU throughout their lifetime [7], and the rate of reoccurrence within the same year of a resolution of a previous ulcer is 40% [8][9]. The complication progression of DFU can lead to devastating consequences such as major limb amputation due to limb ischemia and death. DFU is an economy burden for the healthcare systems being the leading cause of hospital ingress [7]–[11].

According to several studies regular monitorization of the ulcer state, appropriate foot care, and footwear has been demonstrated to improve the patient treatment outcomes and reduce healthcare cost, the need for presential consultations and expensive lab testing [9].

Studies about the correlation between biosensing wound monitoring parameters and DFU prevention and healing evolution have been made about temperature [12], plantar pressure [13], pH [14], moisture [15], bacteria proliferation [16], among others.

Foot skin temperature is a great parameter to prevent the manifestation of DFU, by the detection of inflammation recognized by the local rise of temperature on the area that if un-

treated will develop DFU [12]. When the DFU is already installed, measuring the skin foot temperature and pH of the wound exudate can inform if DFU state is aggravating or healing. The foot skin temperature can be used to identify ulcer infection, by the increase of the ulcer temperature, or ischemia, that is to say lack of blood flow, that can lead to tissue necrosis , by the foot temperature decrease [17]–[20]. Also, the analysis of DFU exudate informs about the wound healing state. An adequate amount of wound hydration is decisive for proper tissue regeneration. A low exudate level can desiccate the wound and slow down the healing, while excess of moisture can lead to its maceration and wound enlargement [15], [21], [22]. Protein degrading enzymes, neutrophils and proinflammatory cytokines present on the wound exudate can increase tissue damage by prolonged exposure time of the wound to its exudate, therefore the change of the DFU dressings is essential for its healing process [22]. Another exudate criteria that dictate the healing state of the DFU is its pH. A pH scale is used to define the acidity or basicity of a solution by indicating the concentration of hydrogen ions in the solution [14], [23]. Through the analysis of wound pH, it is possible to monitor the progression of the DFU. Healthy skin has an acid pH between 4 and 6. After the ulceration and disruption of the epidermis, the pH of the intern milieu is exposed, and it fluctuates around 7.4 pH. When the wound formed is acute the successful healing is characterized by lower basic pH near neutral values and when epithelization occurs the pH drops to acidic values. While on chronic wounds after the wound formation the pH of the wound increase until it fluctuates in highly basic values between 8 and 9 [14], [23]–[25].

Paper-LIG sensors have drawn attention in the electronics industry [26], since LIG is a simple, single-step, fast and high-resolution patterning technique that allows the production of highly conductive, biocompatible and environmentally friendly graphitic material on carbon base materials [27], [28]. Paper in comparison with other substrates used for LIG production such as polyimide (PI), polyethylene terephthalate has the advantages of being economical, abundant, biocompatible, biodegradable and flexible [26], [29], [30]. Additionally, paper as a porous material has a high surface to volume-ratio that allows the immobilization of reagents and passive transportation of liquids by capillary action [31].

Scientists have developed in recent years a big variety of wound healing and DFU monitoring sensors using diverse parameters, fabrication techniques and substrates. However, there is an increasing need from the medical and scientific community for the development of a low-cost, rapid fabrication, biocompatible, environmentally friendly and wearable temperature, and pH sensing device to home-monitor the diabetic foot ulcer healing progression [8], [32]–[34]. Therefore, the motivation of the dissertation work is the development of pH and temperature sensors able to monitor the wound healing state of a DFU, due to the material's exquisite mechanical, thermal and electrochemical characteristics using LIG, a simple, scalable, low-cost and rapid fabrication method, on paper an abundant, biocompatible, sustainable, and economical substrate, able to monitor the wound healing state of a DFU.

1.2. Aim and Dissertation Plan

This dissertation aims to study the application of the LIG fabrication technique on paper for the development of temperature and pH sensors with the possibility of being further integrated into a wearable system able to monitor the DFU healing state. This study started by the evaluation of the effect of laser irradiation had on the paper substrate and a systematic analysis of the LIG electrical, morphology, chemical and structural characteristics with different laser fabrication parameters, through the measurement of the sheet resistance, micro-Raman spectroscopy, scanning electron microscopy (SEM) and energy-dispersive X-ray spectroscopy (EDS). After the study of influence of the laser fabrication conditions on the LIG formed, this material was used with adjusted laser parameters to study its thermoelectric characteristics with the objective to produce sensitive and reproducible temperature sensors. Additionally, the sensor design impact on the electrical performance was studied. Lastly, paper-LIG material was used for the development of the electrochemical cell, that thanks to its scalable characteristic allows the WE modification by electropolymerizing polyaniline (PANI), a biocompatible, low-cost pH sensitive material. The study of the pH sensor electrochemical response was realized by studying the potential variation of the sensor using the open circuit potentiometry measurement method (OCP) to study beyond the sensor response, its reproducibility, repeatability, and long-term stability.

2. THEORETICAL CONCEPTS

This chapter introduces fundamental theoretical concepts that will help to better understand the project work. This chapter explores the sensing material and respective production technique used, the sensors working principles, and physiopathology of the abnormal wound healing of the DFU.

2.1. Graphene

Graphene, consist of a hexagonal honeycomb lattice formed by a monolayer of sp^2 hybridized carbon atom covalently connected by three σ bonds to each other with a remaining π orbital forming a benzene-ring structure [34], as can be seen by the light blue structure on **Figure 1**. Other graphitic allotropes with different dimension can be formed by structurally rearranging graphene, using it as building block [34], [35].

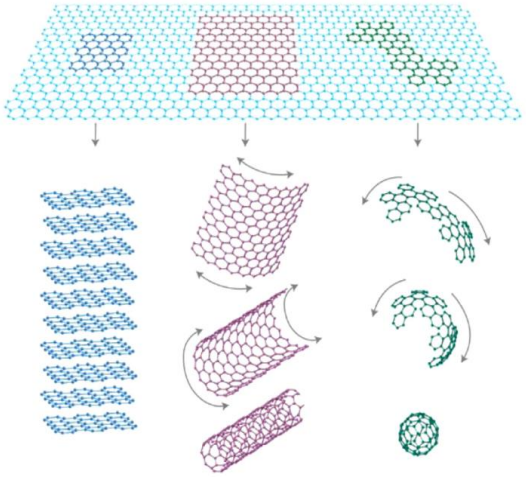

Figure 1 - Graphitic conformations that can be formed by the rearrangement of graphene. If the graphene layers are compiled it forms 3D graphite, the dark blue structure. By wrapping around itself it can form a 0D structure, named fullerene, represented by the green graphene arrangement. And lastly, by rolling the graphene monolayer, the 1D purple nanotubes. Adapted from [35].

The development of new applications and technologies, materials and devices, based on graphene has created a great interest on the scientific community [34], [36]. Once graphene is solely composed of carbon atoms, the most abundant element on the universe and inside all living materials, it demonstrates a huge potential for sustainable and biocompatible applications [34]. This material also has an enormous potential for flexible electronics owing to its high fracture strength, mechanical properties, electrochemically stability and significant piezoresistive performance [34], [36]. This carbon allotrope has as well promising thermal and energy storage applications due to its excellent thermal conductivity, fast mobility of charges carriers, low coefficient of thermal expansion and is the best conductor of heat at room temperature [34], [36]. Additionally, its large surface area, large potential working interval, fast mobility of charges carriers and electronic transfer, easy interaction with biomolecules makes this material very applicable for the development of biochemical sensors [36].

Graphene has multiple traditional production methods such as chemical vapor deposition, mechanical exfoliation, and wet chemical methods, among others [37]–[39]. Most of these techniques, despite their capacity to produce high quality graphene, are not suitable for large-scale production because of lack of efficiency, strict experimental conditions, limitations related to its multiple steps of production and time-consuming [37]–[39].

2.2. Laser Induced Graphene

Laser Direct Writing is a high resolution, mask-less, one step method technology used for engraving and cutting patterns onto the surface of materials with wide freedom of design [28]. In 2014, researchers discovered that it was possible to produce a highly conductive, thermally stable 3D graphene porous structure, through pulsed laser irradiation of the PI film. This material was named Laser Induce Graphene (LIG) [27], [37], [40].

The underlying mechanism of LIG synthesis is that laser irradiation evokes thermally induce lattice vibrations that lead to appearance of extremely high localized energies capable of breaking $C-O$, $C=O$, $N-C$ bonds, followed by the recombination of sp^3 carbon atoms to sp^2 carbon atoms and release of the other elements in form of gases forming stacked graphitic structures (**Figure 2**) [28], [40].

Posteriorly, it was discovered that through the manipulation of the laser production parameters, such as laser power, laser scanning speed, pulses per inch and operational distance and multiple irradiations of the substrate allowed the control of the quality and composition of the porous graphene fabricated [39], [41].

This technique is very versatile, can be used within a wide range of carbon base materials, such as PI, Kevlar, plants, textiles, paper, cork, wood, and other organic films. In comparison with other fabrication methods of graphitic materials, it has advantages that does not require

complex expensive cleanroom equipment, costly materials, or solvents. Additionally its fabrication is characterized by its simplicity and fast production [37]–[39].

Thanks to LIG physical properties its integration on the production of sensors has been widely diverse. LIG has been used to produce piezoresistive sensors, capacitive sensors, triboelectric sensors, electrothermal sensors, gas sensor, magnetoresistive sensors, solar transducer, humidity sensors, electrochemical sensors, heaters and biochemical sensors [37], [39], [40].

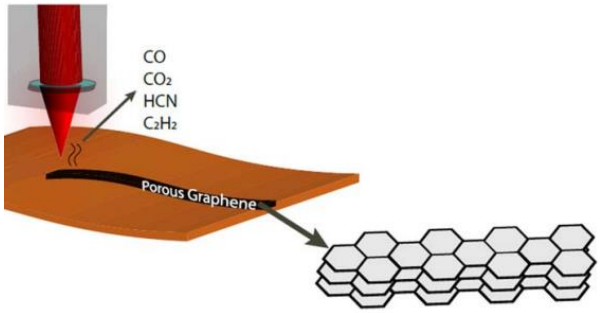

Figure 2 - Representative illustration of LIG formation. Adapted from [28]

2.3. Diabetic Foot Ulcers

DM is a spectrum of metabolic disorders caused by either lack of insulin secretion, decreased sensitivity of the tissues to insulin, or both. DM is characterized by an increase in blood glucose concentration, hyperglycemia, provoked by the increased endogenous hepatic glucose production and/or impaired glucose uptake by peripheral tissues [1], [2].

DM leads to several macrovascular and microvascular complications. Indeed, individuals with a history of DM have a greater tendency to develop ulceration, and destruction of the foot tissue caused by peripheral neuropathy, peripheral artery disease foot deformity and different grades of ischemia and infection, amongst others [5], [42]–[44].

2.3.1. Pathophysiology of Diabetic Foot Ulcers

DFU has neuropathic, vascular and immune system components caused by the hyperglycemic state of DM [5], [42]–[44].

The appearance of DFU occurs by an initial not detected trauma caused by an existing peripheral neuropathy [5], provoked by oxidative stress on nerve cells caused by hyperglycemia [4].

Peripheral neuropathy

Peripheral neuropathy is a microvascular complication of DM, that affects sensory, motor, and autonomic nerves. Sensory neuropathy modifies the patient's ability to perceive pain, temperature, pressure, and touch making the foot vulnerable to traumatic damage. Motor

neuropathy causes an imbalance of the foot biomechanical forces, altering the foot anatomy by developing atrophy of the foot muscles, toe deformities, and limited joint mobility. These alterations evoke the formation of callus, which in turn facilitates the ischemic necrosis of the tissues near the callus leading to loss of skin and subcutaneous tissue. Autonomic neuropathy impairs microvascular thermoregulation, reducing sweating and increasing temperature, predisposing to dryness and fissuring and potential entry for bacteria [2], [5], [42], [44].

Peripheral Arterial Disease

Peripheral Arterial Disease is a risk factor for the DFU development [5]. It is characterized by atherosclerotic occlusive disease of the lower extremities caused by the altered glucose metabolism of DM that provokes arterial stiffness, thrombotic abnormalities, low-grade inflammation, and endothelial cell disfunction that leads to the decrease vasodilators, consequently resulting in vasoconstriction and plasma hypercoagulation that lead to ischemia [42]–[44].

Diabetic Immunopathy

Individuals with DM are highly susceptible to suffer from infections due to prolonged exposure of the wound where hyperglycemia promotes the colonization of a variety of organisms and abnormal cell-mediated immunity [2], [5]. The mechanisms that characterize their de-efficient immune system are impairment of cytokine production, leukocyte recruitment inhibition, defective pathogen recognition and neutrophil, macrophage, and natural killer dysfunction and inhibition of antibodies and complement effector [5], [45].

2.3.2. Diabetic Foot Ulcer Classification

When monitoring the wound healing process of DFU, it is important to be aware of the natural progression of the diabetic foot whose severity depends on several factors such as the presence and depth extension of wound, level of ischemia and foot infection [4], [46], [47]. The progression of the DFU can be representatively summarized in 5 stages. The first stage consists of individuals that suffer from DM disease, with healthy feet that don’t present any risk factor associated with DFU development. The second stage corresponds to DM patients that present sensory, motor, or autonomic neuropathy symptoms, such as lack of sensation of the feet, deformities or callus formation and abnormal thermoregulation symptoms respectively, or ischemia, but don't have any injury. The third stage corresponds to DM patients that developed an ulcerated foot. The fourth stage occurs when there is an infection of the foot ulcer. And finally, the fifth stage is marked by the emergence of necrotic tissue on the infected foot [4], [46]. It is of major importance to prevent ulcer formation of DM patients between the first and second stages. However, after the ulcer is installed its wound healing monitoring is essential to avoid the DFU progression to more severe stages. When a DFU

creates necrotic tissue, it means that the wound cannot heal and the only way to save the patient life is amputation [46].

2.3.3. Wound Healing & Diabetes Mellitus

Diabetic wounds do not follow the normal wound healing process, as can be seen by **Figure 3.** A brief description of each phase and corresponding DM alteration will be presented.

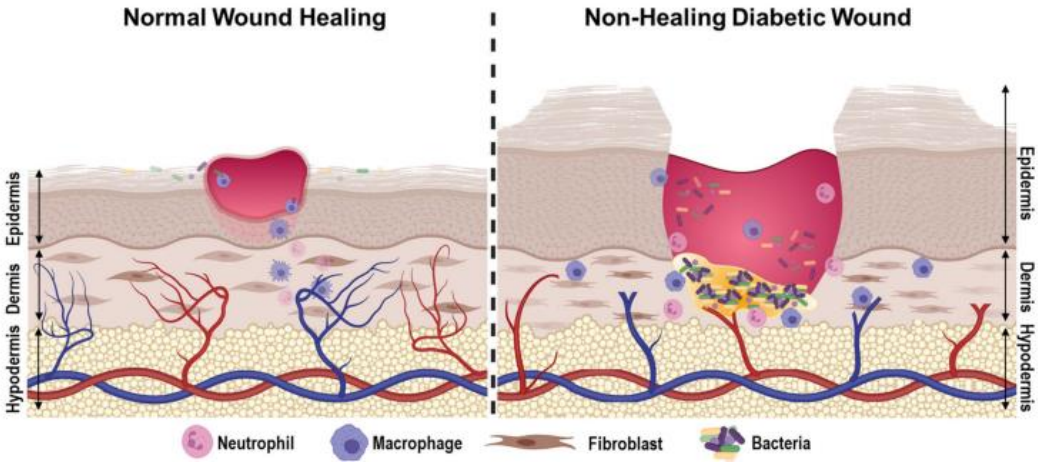

Figure 3 - Representation of the physiological differences between the wound healing process of a healthy individual and the wound healing process of an individual with DM. The representation of the wound site of an DFU demonstrates the destruction of deeper skin layers, a persistent bacterial colonization, less blood irrigation, and prolonged inflammation phase, represented by the higher number of macrophage, and neutrophil on the wound site [48].

Hemostasis

After the skin integrity is lost and resulting bleeding from the injury site occurs, the hemostasis process is activated by provoking vasoconstriction and platelets activation, aggregation and adhesion to the damaged endothelium occurs to prevent exsanguination and to form a temporary extracellular matrix fibrinogen is converted to fibrin to form the provisional extracellular matrix. Individuals with DM at the hemostasis phase experience hypercoagulability and reduced fibrinolysis [5], [23], [49].

Inflammation

After the coagulation of the injury properly occurs, the aggregated platelets within the clot, neutrophils and monocytes at the wound site area recruit inflammatory cells as neutrophils, monocytes through the release of pro-inflammatory cytokines and various growth factors, which are essential for the wound healing process. This phase usually initiates a few hours after the injury and last on average 72 hours [5], [23]. The healing process in DM pa-

tients is mainly characterized by the maintenance of a prolonged inflammatory response, marked by elevated levels of the cytokine interleukin 1β (IL-1β) and tumor necrosis factor α (TNFα) for longer time than the inflammation phase usually occurs. Also its macrophages exhibit impaired phagocytic activity and its neutrophils have impaired function resulting in failure tissue repair [5], [23], [49], [50].

Proliferation and Migration

At the proliferation phase, the appearance of myofibroblast that cause wound contraction, angiogenesis, increase production of collagen, fibronectin and, migration of keratinocytes and extracellular matrix regeneration by the formation of granulation tissue occurs [5], [23]. On DM individuals this phase is compromised by diminished angiogenesis and reduced levels of insulin like growth factor-1 (IGF-1), essential factor for cell-granulation and wound re-epithelization, and transforming factor-β (TGFβ), responsible for the recruitment and migration of immune cells, keratinocytes, fibroblast and vascular cells, causing an abnormal re-epithelization [5], [49], [50].

Remodeling Phase

In this wound healing phase, the collagen is replaced by the degrading collagen III, also it occurs the maturation of the blood vessels and degradation of the temporary extracellular matrix that was formed at the hemostasis phase. The granulation tissue formed increases the wound resistance ending in the scar formation [5], [23]. DM patients endure reduced levels of TGFβ and imbalanced levels of the tissue metalloproteinases and its inhibitors, affect the regulation of extracellular cell matrix [5], [49].

2.3.4. Wound Healing & Diabetic Foot Ulcers

Wounds can be classified as acute or chronic according to the efficiency of their healing process. Acute wounds heal within a predictable period, while chronic wounds have a slow progression through the healing phases, that corresponds to category DFU is usually inserted. Wound infection occurs when there is no microbial balance, and the microorganism present within the wound causes local tissue damage and impedes wound healing. Wound infection intervention is of great importance to assist the host defenses to destroy the invading microorganisms. Monitoring the wound state and features such as its pH and temperature, is essential on both wound categories to prevent and control infections [51], [52].

pH

According to several studies, there is an apparent correlation between the wound exudate pH, temperature and its wound healing state [53]–[55].

The regulation of pH changes may alert for biochemical reactions and cellular processes related to the wound healing state. Several studies have analyzed the presence of enzymes

that contribute to wound healing, and proliferation of certain microorganisms present on infectious stages at different pHs [25], [56]. Also, pH has been demonstrated to be a good indicator to categorize the wound and follow the healing progression, since acute wound and chronic wound evolution of pH values differ significantly, as explained by **Figure 4** and **Figure 5** [14], [23], [24].

The skin works as a microorganism barrier, so its pH fluctuates between the pH acidic values between 4 and $6\ pH$. When an injury occurs, there is the alteration of the natural acidic milieu of the skin by the destruction of multiple dermal layers, that exposes the internal tissues and internal fluids with the neutral pH of 7.4. Consequently, if the wound generated is classified as acute the wound milieu starts with a neutral pH. When wound healing process of the acute wounds achieves an effective re-epithelization phase the pH of the wound milieu diminishes, returning to acidic values [14], [23], [24].

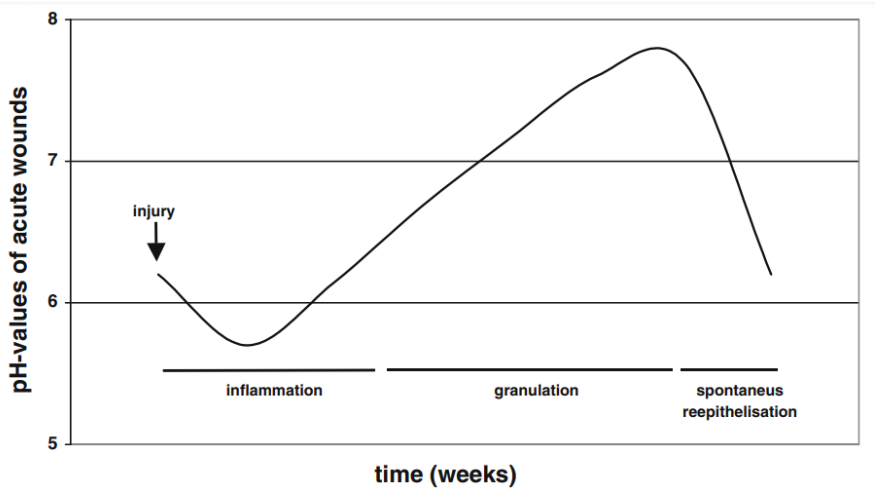

Figure 4 - pH value evolution through the wound healing process of an acute wound. Image adapted from [14]

In contrast, if the wound healing is delayed, the pH will oscillate between alkaline values over time, which corresponds to chronic wounds, whose pH are between 7.15 pH and 8.9 pH, but has been reported wound exudate cases with 9.5 pH [14], [23]–[25][25] .

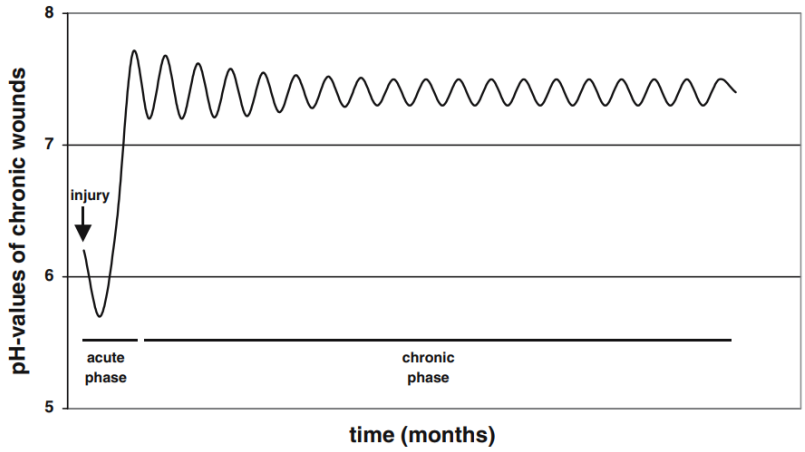

Figure 5 - pH evolution of the wound healing process of a chronic wound. Image adapted from [14]

Temperature

The thermal regulation of the skin may vary with ischemia and neuropathy pathologies and peripheral arterial disease [18]. The assessment of subtle changes in the thermal pattern of the foot could help identify the DFU state.

Some studies have detected early stages of the development of DFU, through the identification of the inflamed area marked by the temperature increased one week before DFU appears [57], [58].

After the DFU is installed, thermal monitorization can identify an early stage of infection before other secondary symptoms appear, once the ulcer inflammation anticipates wound infection, through the ulcer temperature raise. The range temperature of an infected wound is from 38 to 42ºC [58]. Infections are classified as hotspots, erythema and foot ulcers whose temperature difference with contralateral foot is of 2.2ºC [57].

Additionally, by measuring the temperature of the ulcer it could be possible to identify ischemia [18] and necrosis by the ulcer temperature decrease [20]. Once ulcers characterized by lower temperature than adjacent skin are approximately 32 times more likely to progress to necrosis than ulcers with higher temperature than adjacent skin [20]. Studies have demonstrated that a temperature decrease of 2.2 ºC indicates that the wound is likely to suffer local ischemia [19], [59], [60].

Several studies are searching for the correlation between the plantar foot temperature and individuals with different characteristics, such as presence of neuropathy, previously healed ulcers and individuals who suffer previous toe amputations. The most relevant conclusions made were that individuals with neuropathy and past ulcer and individuals with neuropathy have higher foot temperature than individuals without neuropathy [12], [61], [62]. The temperature ranges for each group were from 32 to 35 ºC and 27 to 30 ºC, respectively [62]. Additionally on a study focused on bilateral temperature asymmetries between the right and left feet observed that DM patients with no complications had temperature difference of less than 2ºC while, temperature superior to 2ºC meant patients presented complications

[18], [57]. Additionally, it is possible to distinguish between local complications and diffuse complications. For instance, a difference in temperature between the contralateral foot superior to 2ºC, implies that the patient has developed local complications. However, if the temperatures difference is greater than 3ºC, this suggests that the patient has developed diffuse complications [18].

2.4. Biosensors

Biosensors have an important role in a wide range of areas such as point-of-care monitoring of treatment and disease progression, environmental monitoring, food control and biomedical research [63]. A biosensor is a device that converts a physical phenomenal or chemical reaction into a measurable signal that indicates the phase of a specific biological event. Biosensors are usually composed of a bioreceptor and a transducer. The bioreceptor is a biomolecule that recognizes the chemical substance of interest, also known as the analyte, and binds to it. The transducer converts the recognition event to the emission of different physical measurable signals such as light, heat, pH, charge, or mass change. After the signalization the transduced signal is amplified and converted into digital. The data is exhibited with a user interpretation system that can display the data in the form of a graphic, a table or a figure. We can classify biosensors in several categories according to the characteristics of their bioreceptor, the characteristics of their transducer and the detection system [64]–[66].

2.4.1 Temperature Resistive Sensors

Temperature sensors play a key role on health monitoring devices, personal healthcare, and disease diagnosis [67].

Thermodynamics defines temperature as a function of the average kinetic energy of the vibrating particles of an object. However, the molecular movement is hard to measure directly, so temperature sensors are generally designed to measure a physical property that changes in response to temperature [68].

Temperature sensors can be divided into thermoresistive, thermoelectric contact sensors, piezoelectric temperature sensors, semiconductor pn-junction-based, and acoustic. The most popular temperature sensors are the thermoresistive, semiconductor pn-junction, and thermocouples [68], [69]. The temperature sensors developed in this dissertation are thermoresistive.

Thermoresistive sensors are made of sensitive materials that change their electrical resistance with temperature. Some of the advantages of this type of sensor consists of its high sensitivity and long-term stability and ability to form simple interface circuits. This kind of

sensors can be divided into resistive temperature detectors (RTD), thermistors, and silicon resistive [68].

A brief explanation about the physical phenomena that justifies the behavior and sensitivity of the materials that compose the temperature sensors will be presented.

The electrical resistance changes caused by the influence of the temperature change is known as the thermoresistive effect [70]. The resistance alteration (ΔR) due to temperature variation (ΔT) is conditioned by geometric effects (α) and the change in resistivity (ρ) [70].

$$\frac{\Delta R}{R} = \frac{\Delta \rho}{\rho} - \alpha \Delta T$$

An important physical concept for thermoresistive sensors is the temperature coefficient resistance (TCR), also known as thermoresistive sensor sensitivity. It is a material property defined as the change of resistance in function with temperature, expressed by ppm°K^{-1} [68]. However, the units used to classify the sensitivity of the thermoresistive sensors developed in this dissertation for simplicity and popularity purpose were %°C^{-1}. The geometric effect can be neglected on most cases, because it doesn't affect significantly with the calculation of TCR [70]. This coefficient is simplified by the following equation:

$$TCR = \frac{1}{R_0} \frac{R - R_0}{T - T_0}$$

Where R_0 is the resistance at room temperature, T_0 ,and R is the resistance at operating temperature, T. Sensors can be characterized by a positive temperature resistance coefficient, represented by PTC or a negative temperature resistance coefficient represented by NTC. Materials with large TCR are used to fabricate thermoresistive sensors such as thermistors and resistive temperature detectors [70].

On semiconductor materials the thermoresistive effect arises because temperature affects the mobility and number of carriers in the conducting material. On crystalline materials, with the rise of temperature there is an increase of the free charge carriers as they are thermally excited, which leads to an increase of electrical conductivity. On the other hand, scattering effect and lattice vibrations, provoked by the increase of temperature, diminished the mobility of the carriers. Consequently, when the temperatures suffer an increase the resistivity of semiconductors can increase on PTC sensors or decrease on NTC sensors, according to the change in the number of carriers and their mobility [70].

The variation of the resistivity of the semiconductors can be represented by the graph on **Figure 6**, that can be separated in 3 regions. The extrinsic region that appears at low temperatures is characterized by a decrease of the electrical resistivity provoked by the generation of more carriers by thermal energy, and the lattice scattering causes a slight reduction of mobility. At higher temperatures, the semiconductor is at the Metal-like region, on which occurs the saturation of the free carrier's concentration and the carrier's mobility decreases. And lastly, at the highest temperature range the semiconductor is in the intrinsic region, defined by the rupture of a significant number of bonds increasing the carrier's concentration and decreasing the resistivity in this region [70].

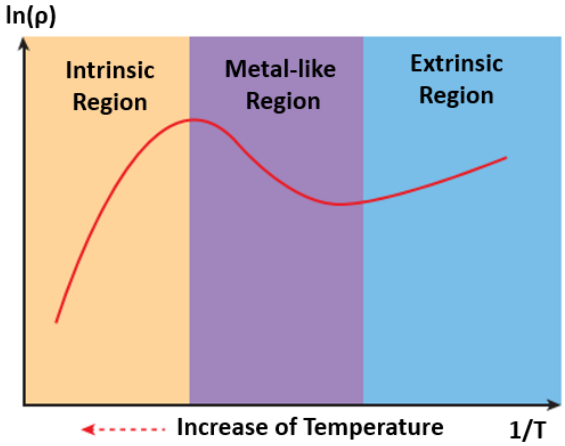

Figure 6 - Evolution of the resistivity of a semiconductor with temperature.

While in metals the thermoresistive effect acts differently. With the increase of temperatures there is no generation of carriers, the electron concentration in metals is constant. However, the temperature increase provokes the reduction of the charge carrier's mobility resulting in a linear increase of the materials electrical resist, given by the following equation [70]:

$$R = R_0\left(1 + TCR\frac{T - T_0}{T_0}\right)$$

Next, the characteristics of the thermistor and RTD will be described. Thermistors are defined by large NTC or PTC with nonlinear temperature-resistance characteristics. They are composed of ceramic semiconductors metal oxides, normally nickel, manganese, cobalt, titanium or iron. [68], [70]. Thermistors possess nonlinear temperature resistance characteristics. On the other hand, RTD are usually composed of metal and some semiconductor materials such as germanium sensors fabricated in the form of either a wire or a thin film. Platinum is the most used material, because of its predictable response, long-term stability, and durability [68], [70]. The resistance variation of Platinum RTD is represented by the Callendar-van Dusen equation for the range of 0℃ to 630℃ :

$$R_T = R_0[1 + AT + BT^2]$$

Where R_T is the resistance of the platinium RTD at the temperature T, R_0 is the calibrating resistance at 0℃ [70].

2.4.2. Electrochemical Potentiometric Sensors

Electrochemical sensors are the most investigated and used biosensor, due to their versatility, high sensitivity and direct measurement [68]. They can be divided into potentiometric, amperometry and conductometric, by their operating mode that consists of the measurement of the voltage, electrical current and conductivity or resistivity, respectively.

The operating principle of an electrochemical sensor relies on the study of the electrochemical reaction, that involves the transfer of charges, between the electrode and solution interface on the electrochemical cell. An electrochemical sensor requires a closed circuit

to flow the electrical current to make a measurement [68]. Therefore, the electrochemical cell needs at least two electrodes, although it is usually composed of three electrodes [64].The working electrode (WE) is the most important component of the sensor because it is where the targeted chemical reaction of oxidation or reduction occurs [68], [71], [72]. The reference electrode (RE) has a well-known and fixed electrochemical potential. So the potential change observed is attributed to the WE [68], [71], [72]. This electrode is most commonly modified with Ag/AgCl for aqueous solutions because it offers a stable potential profile and is practical and environmentally friendly [68], [71]–[75]. The counter electrode (CE) is used to complete the circuit flow, it doesn't participate in the chemical reaction it only operates to induce the passage of electrical current through the solution [68], [71], [72]. The surface area of this electrode is much larger than the WE to prevent kinetic limitations on the reaction [76]. Also, RE must be of a non-reactive material [72]. The electrodes can be modified to improve the electron transfer properties between the chemical species involved [68].

The electrochemical reaction that occurs on the WE interface, and solution is given by the simple reversible redox reaction represented by the following equation:

$$O(aq) + ne^{-} \rightleftarrows R(aq)$$

Where O is the oxidized species that by acceptance of n electron is reduced forming the chemical specie R. The electrons of the electrochemical cell are submersed in the solution, a medium that carries charges, the CE acts as an electron source, as the electron transfer moves towards equilibrium a potential difference is created between the WE interface and the solution [72], [77]. Through the incorporation of the RE with fixed potential, the potential of the WE can be measured through the Nernst Equation:

$$E = E^{0} + \frac{RT}{nF}\ln\left(\frac{[O]}{[R]}\right)$$

Where E is the electrochemical cell potential. E^{0} is the standard cell potential, T is the temperature during the measurement, R is Universal gas constant, F is Faraday's constant, n is the number of electrons transferred and $\frac{[O]}{[R]}$ is the concentration ratio between the oxidized specie and the reduced specie. The Nernst Equation is the base concept of potentiometric sensors [72], [77].

The principle of operation of potentiometric sensors is based on Open Circuit Potential measurement techniques also known as zero-current potential, equilibrium potential or rest potential is a passive technique where the potential difference between the WE and the fixed potential of the RE is measured, when the current flow is equal or near zero, that is in equilibrium or quasiequilibrium conditions, respectively [68], [71], [72], [78]. The potentiostat at OCP technique works as a voltmeter, as it can be simply defined by the potential difference between the WE and RE. A constant OCP is an indicator of electrochemical stability of a system on a perturbation-based experiment [78].

A potentiometric pH sensor measures the difference in electromotive force between the WE composed with a pH sensing substance and the RE [73]. A frequent method for

measuring pH is the use of potentiometric glass electrodes in pH cells. However, glass electrode measurements are affected by high temperatures, show acid-base error and high impedance and difficulty in miniaturization, which limits their further application [79], [80]. Recently the scientific community has developed flexible, solid-contact pH sensors capable of replacing the glass pH electrodes [80], [81].

The pH of a solution can be measured by performing the OCP with a potentiometry sensor, by using the *Nernstian* equation:

$$E = E^0 - 2.3\frac{RT}{nF}\mathrm{pH} \Leftrightarrow E = E^0 - 0.5914\mathrm{pH}$$

The sensitivity performance of potentiometric pH sensor is given by the slope of the linear regression of the standard calibration line that can be approximated to the *Nernstian* equation, that is, is determined by the similarity of the sensitivity factor with the ideal *Nernstian* response given by $59.14\ mV/pH$ at 25℃ [82], [83].

2.4.3. Flexible and Wearable Sensors

Thanks to the technological advances on the flexible electronic and nanotechnology fields, the development of wearable and flexible sensors have received tremendous attention by functionalizing materials with inherent flexibility and stretchability [40], [80], [84]. These sensors can provide real-time personalized physiological information for health monitoring and health status of individuals from continuous monitoring of biochemical markers in biological fluids, such as tears, sweat, saliva and wound monitoring, but also physical markers, such as temperature, pressure, flow, among others [80], [85], [86]. In comparison with sensors with rigid electronic materials, flexible and wearable sensors are less affected from motion artifacts and mechanical mismatches, also they don't limit the user mobility and comfort [80], [84]–[86]. Real-time health care monitoring can be very useful in early prediction and treatment of various diseases [80], [85]. In the context of wound care, this technology has been incorporated in wound dressing to develop point-of-care platforms [33], [87].

3.

STATE OF ART

DM patients due to peripheral neuropathy frequently do not perceive the signs and symptoms of ulceration and DFU infection. Therefore, clinicians have an increasing need for rapid and accurate estimation of the wound state and trajectory to make timely interventions, especially because DFUs have a higher tendency to develop infections that can lead to severe consequences such as major amputation or death [25], [88].

As the scientific community recognized this major necessity, several investigation groups have developed monitoring devices for wound healing integrating biochemical markers such as pH, cytokine, enzyme, metabolic byproduct, and others; and physical markers such as temperature, pressure, moisture level, and others [6], [33], [89]. The goals of this chapter are to give some insight into the sensors that have been developed by the scientific community to measure the physical properties of temperature and pH through the technique of production used in this dissertation. And lastly, give a small presentation of projects developed to monitor the healing process of wounds.

3.1. Temperature Sensors

Graphene, on different fabrication methods has been used to develop graphene thermoresistive sensors. Liu et al. in 2019 [67], fabricated a disposable, low cost temperature sensor by directly writing or mask spraying highly thermo-sensitive graphene nanoribbon ink on commonly-used paper. The sensor sensitivity is $1.27\%℃^{-1}$ in the temperature range of $30℃$ to $80℃$, it has high cyclic resolution, 0.5 s response time, and its temperature resolution is of $0.2℃$. This sensor was applied to sense body temperature, but it was also sensible to touch and could be used to monitor respiratory rate. Also Gong team [67] in 2020 developed a temperature sensor composed of polyethyleneimine and reduced graphene oxide bilayer on PI substrate by spray dipping, the sensors sensitivity is $1.30\%℃^{-1}$ its linearity is $R^2 = 0.999$ and accuracy of $0.1℃$ and a 60 day durability on the temperature range between $25℃$ and $45℃$. In 2022, Štulík et al. [90] made a comparatively study of the thermoresistive behav-

ior and its humidity dependance of graphene sensors with different production techniques, respectively using chemical vapor deposition of graphene on polycrystalline copper foil, reduced graphene oxide and graphene nanoplatelets using alumina plate with gold interdigital electrodes as substrate and graphene grown from plasma.

The scientific community, by perceiving the potential of the LIG technique, have made studies analyzing its behavior for the development of thermoresistive sensors. Such as the project made by Kun et al. [91], in which they produced a LIG temperature sensor on PI substrate, patterned with a CO_2 laser. The sensor demonstrated high accuracy, of ± 0.15℃, linear response whose sensitivity was $-0.042\%℃^{-1}$. On the same year Han team in 2021 [92], proposed the fabrication temperature sensors using a sensitive layer of reduced graphene oxide and LIG for the electrode area on a PI substrate. The sensor developed showed a high sensitivity of $1.56\%℃^{-1}$ within the temperature interval of 25 and 45°C with a resolution of 0.2℃, and 13.5 s of response time. Lastly in 2022, Kulyk's team [93], produced LIG on paper temperature and humidity sensors with UV laser irradiation. The sensitivity of the temperature and humidity sensor was $-0.28\ \%℃^{-1}$ and $1.3 \times 10^{-3}\ \%RH^{-1}$, respectively on the following temperature and humidity intervals 10℃ to 60℃ and $10\%\ RH$ to $100\%\ RH$. Both sensors demonstrated high linearity. The resistance of the LIG produced was bellow $125\ \Omega sq^{-1}$.

Temperature sensors have been incorporated on skin monitor devices that communicate wirelessly to a smartphone application. On 2019 Gandla et al. [94] developed a wearable, on-skin device able to monitor temperature in real time that incorporated a flexible temperature sensor, a multilayer biocompatible patch to attach the device on the body zone of interest, flexible printed circuit boards that integrates a customized signal processing integrated circuit, a wireless communication system via Bluetooth and a battery, and a custom built smartphone android application. The sensitive material on the temperature sensor was LIG on Kapton PI films with $200k\Omega$ of resistance, TCR of $0.142\ \%℃^{-1}$ in the temperature range -10℃ to 60℃ with 5℃ with highly linear $R^2 = 0.999$ and stable responses. Additionally, the sensor performance did not alter significantly with relative humidity. In 2020 Pang et al. [58] developed a smart flexible device to be incorporated on the wound dressing to monitor the temperature of the wound and predict its infection, and release from an antibacterial UV responsive hydrogel. Zhang and team [95], in 2021 monitored a wound temperature to predict the formation of wound infection, through a sensing platform. The platform developed by these group is composed by a flexible sensor chip composed by heart rate, blood oxygen saturation sensor, pressure sensor, temperature and humidity sensor, pH sensitive membrane and power management on PI substrate, a controlled printed circuit board composed by the power interface, digital controller, bluetooth antenna, and a customized smartphone application to receive and display data from the sensor. The range of temperature measured by the device was between 35°C and 42°C. It exhibits good long-term stability, an accuracy inferior to 0.3 ℃ and a response time lower than 30 seconds. The device was subsequently used to

study wound infections on rabbit models, by studying the temperature changes on the simulated wounds with different pathogens.

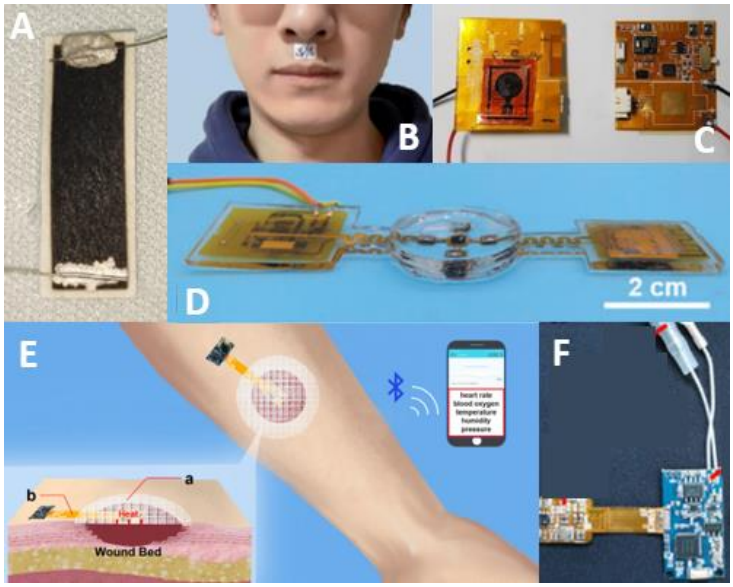

Figure 7 - **A)** Paper LIG temperature and humidity sensor (adapted from [93]). **B)** Temperature sensor of graphene nanoribbons on paper (adapted from [67]). **C)** Skin temperature monitoring device with LIG on PI sensor LIG (adapted from [96]). **D)** Wound Infection temperature monitoring device with drug-delivery (adapted from [58]). **E)** Prototype Wound Healing Monitoring device with incorporated temperature sensor and respective device **F)** (adapted from [95]).

3.2. Potentiometric pH Sensors

PANI has been widely used on WE of pH sensor, thanks to its chemical stability, low cost, ionic and electron conductivity, and principally high pH sensitivity. Once the pH sensor developed in this dissertation used PANI as pH sensitive material, a brief literature review of potentiometric sensors with this material will be presented.

In 2019, Park's group [73] reported the development of a flexible potentiometric pH, whose sensitivity was $62.4\ mVpH^{-1}$ from 3.9 pH to 10.1 pH, 12.8 s of time response, repeatability of 97.9% and durability of $3.0\ mVh^{-1}$. The sensor was constructed on flexible polyethylene terephthalate substrate. Ag/AgCl and carbon paste were screen printed on the RE and WE, correspondingly, and posteriorly the WE were polymerized with aniline forming PANI.

Moreover, scientific groups have incorporated the LIG technique on the electrode production of PANI potentiometric pH sensors. Examples of studies that incorporated LIG technique are Xuang team in 2018 [97] produced a LIG electrochemical pH sensor on a PI substrate and transferred to a substrate made of silver nanowires and silicon base (PDMS). The WE were coated with a PANI membrane and Ag/AgCl paste was cast on the RE. The sensor sensitivity between 4 pH and 7 pH was $66\ mVpH^{-1}$. More recently, in 2022 Liao et al. [98]

produced a flexible and wearable potentiometric pH, Na^+ and K^+ sensor. The electrodes of the pH sensor were fabricated using LIG technique on PI substrate, then PANI is electrodeposited on the WE and Ag/AgCl paste is drop-coated in the RE. The sensor demonstrated good reproducibility and stability. The pH sensor sensitivity was of 51.5 $mV/\,decade$ from 4 pH to 7 pH.

Interesting approaches have also been made to integrate potentiometric pH sensors on commercial bandages to supervise the wound healing state. In 2014, Guinovart et al. [99] developed a wearable, potentiometric pH sensor to monitor the wound pH. The electrodes used were screen-printed and posteriorly incorporated onto commercial bandages. The conducting polymer used for pH sensing on WE were electropolymerized PANI. The sensor can measure from 5.5 pH to 8 pH, and its sensitivity is 59.2 $mVpH^{-1}$.

In 2018 Pal et al. [100] developed a wearable pH monitoring sensor that could be incorporated within commercial bandages to detect the status of chronic wounds. The sensor was fabricated on treated Whatman paper substrate and PANI the sensitive material used was laid on the substrate through stencil printing. Pal's team also Later, the sensor performance was tested in an *in vivo* rodent model to detect the ulcer formation.

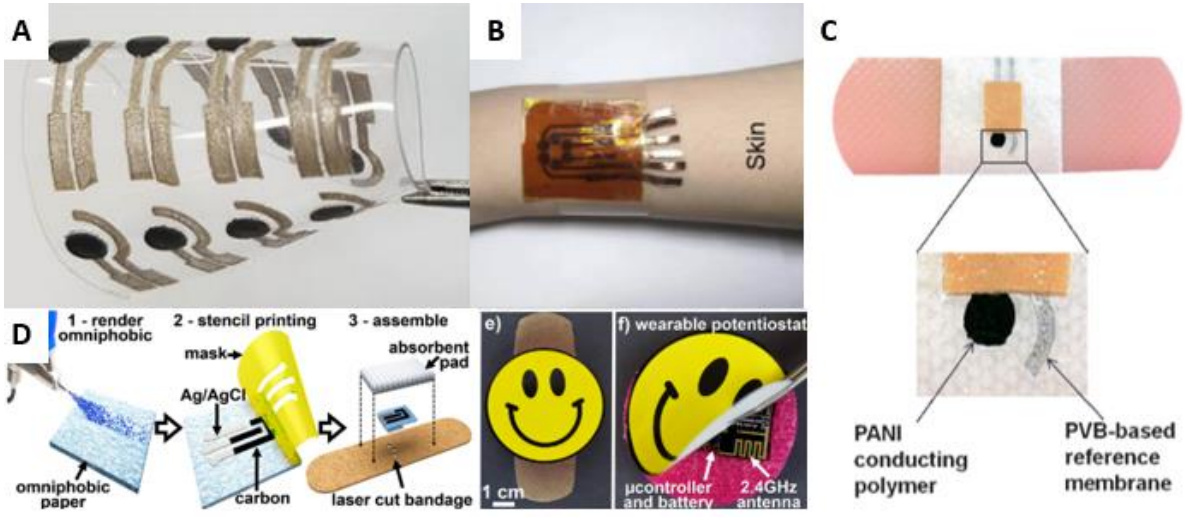

Figure 8 - **A)** Flexible pH potentiometric sensor (adapted from [73]). **B)** Wearable pH potentiometric sensor to measure sweat pH (adapted from [98]). **C)** pH potentiometric sensor on a commercial bandage to measure wound pH (adapted from [99]). **D)** pH potentiometric sensor incorporated on commercial bandage and wearable potentiostat (adapted from [100]).

Nevertheless, it is possible to verify that not all the sensors presented used simple production methods, or the materials used were eco-friendly. There is a huge burden of aged electronic devices causing pollution and health hazards to living beings. Therefore, the approach used in this dissertation project to develop a temperature and pH sensors uses LDR, a simple and cost-effective approach that allows the patterning of several devices, exhibiting different shapes and configurations, while producing a minimum of waste. The choice to use paper as the substrate and LIG as the conducting material is a very interesting combination

to fabricate flexible, biodegradable low-cost devices with significant performance devices [29], [93], [101], thanks to LIG's advantageous properties, like higher mechanical strength, excellent flexibility, and higher conductivity [36], [40]. Additionally, the work of this dissertation is included on a Santander-winning project, whose aim is to develop an environmentally friendly smart bandage to monitor DFU healing state through the incorporation of paper-LIG sensors. The sensors developed will be posteriorly tested on *in vivo* rodent models [102].

4.

MATERIALS AND METHODS

This chapter presents the materials and equipment used for the fabrication and characterization of the sensors developed on this dissertation, followed by the experimental procedures of fabrication and characterization of the LIG produced and lastly temperature, humidity, and pH sensors optimization.

4.1. Materials

The LIG sensors developed in this dissertation used Whatman chromatography paper grade 1 (Whatman International Ltd., Florham Park, NJ, USA) as substrate.

The paper posteriorly suffers a chemical treatment using a solution of sodium tetraborate decahydrate attained from Sigma and ultrapure Mili-Q water laboratory grade.

Later the treated paper was wax printed with the Xerox ColorQube printer.

After the LIG is produced on the substrate, to ensure that the quality of the graphene produced is not altered by the environment humidity, temperature, and pH sensors are encapsulated and sealed in A6 glossy plastic laminating pouches (Staples Europe BV., The Netherlands). The electrical contacts are painted with silver conductive ink (AG-510 silver ink, Conductive Compounds, Inc, Hudson, NH).

The connection between the electrode area of the thermoresistive sensors electrodes and the crocodile tips of the electrical characterization equipments used to study the sensor resistance while variating the temperature and the sensor resistance with relative humidity was assisted by the incorporation of copper adhesive tape or silver wires.

The solutions to modify the WE of the pH sensor were produced with Milli-Q water laboratory grade and the chemicals used, aniline ($C_6H_5NH_2$) and hydrochloric acid (HCl) were both purchased from Merck.

The buffer solution to test the pH sensor was also prepared with Milli-Q water laboratory grade, acetic acid (CH_3COOH) was acquired from Merck, phosphoric acid (H_3PO_4) from

Honeywell, boric acid (H_3BO_3) from Sigma-Aldrich and sodium hydroxide ($NaOH$) from Labkem. All chemicals used were not further purified.

4.2. Experimental Fabrication Equipment

4.2.1. Commercial CO_2 Laser

The equipment used to produce the LIG on the paper sensors was the commercial CO_2 laser at the Center for Materials Research (CENIMAT|i3N) at Nova University Lisbon, **Figure 9**.

Figure 9 - Universal Laser Systems VLS 3.50 CO_2 commercial at CENIMAT|i3N

The system behind its functionality consists in a pulsed cutting laser associated with a plano-convex lens of type 2.0 forming a beam with 10.6 μm of wavelength, and 50 W [103].

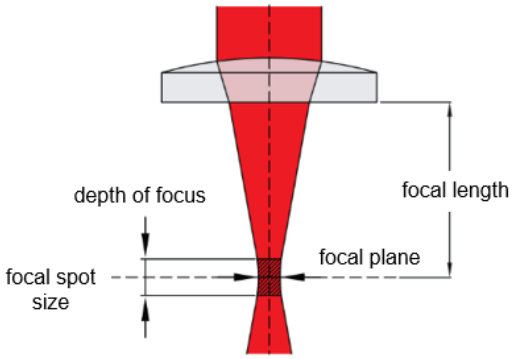

Figure 10 - Schematic adapted from [104] of the optical system of the laser beam formed with the following characteristics: depth of focus of -2.54 mm, focal length of 50.8 mm, spot size of 0.127 mm,

The desktop laser includes a computer interface that grants the user the power to control the laser settings respectively, the laser power, laser speed, and laser repetition rate.

To engrave or cut a material with a specific design, the user should upload a vectorial image with the color map red, green and blue (RGB) with the desired design. The designs

inputted must be made with the 8 colors shown at **Figure 11**. Each color encodes a combination of the laser mode, power, speed, pulse frequency of the laser.

The objects in a design can be of two kinds, vector objects or raster objects. Vector objects consist of any element if their line has less than $0.0254\,mm$ of thickness, every other object is considered a raster object [103].

The laser has 3 modes of operation. Rast mode marks or engraves into the material through the production of a series of pulses in a zig-zag trajectory forming row by row the full design. Vect Mode, the laser follows a two-dimensional path cutting or marking a shape into a material by applying an incident ray in a movement following the lines of the design. Skip mode cause all the elements of the design mapped to that color to be ignored [103].

The user can choose the percentage of the laser power and speed from 0.1% to 100%. At the Power setting corresponding to $0.05\,W$ to $50\,W$. The higher the power applied, the deeper it engraves or cuts. The correspondence of percentage of processing speed varies from the mode of operation. At Rast mode it is from 0.127 to $127\,cms^{-1}$, and at Vect mode it is from 0.0254 to $25.4\,cms^{-1}$. Additionally, the user can also set the pulse frequency of the laser from 1 to 1000 pulses per inch (PPI). Higher PPI can the melted, burned or charring edges, while lower PPI have this effect reduced, the edges can appear with a serrated look [103].

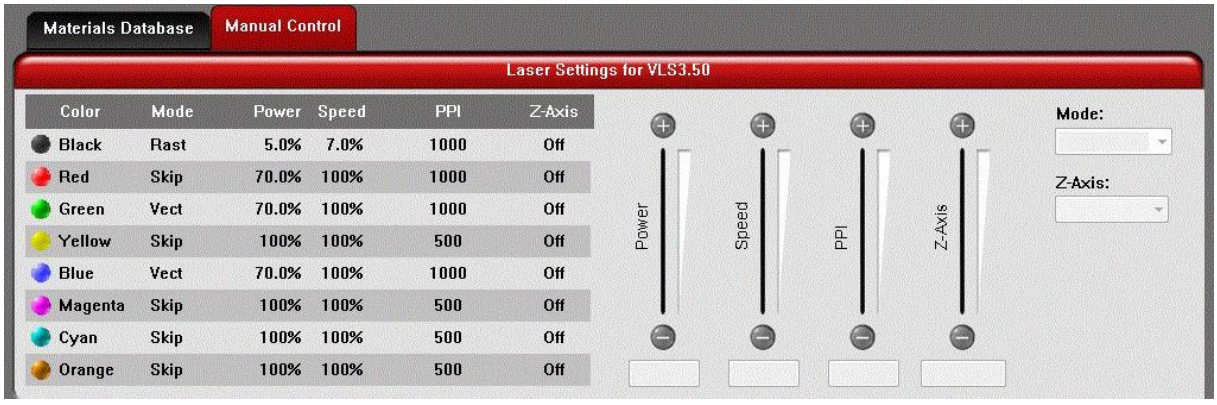

Figure 11 - Laser Interface window to choose the settings of the laser system.

The laser is composed by the laser source, the system with three mirrors that guide the laser to a focusing lens and the moving stages that allow the laser movement in the axis X and Y forming the desired pattern. The movement with the Z-axis occurs by moving the platform that holds the substrate **Figure 12**.

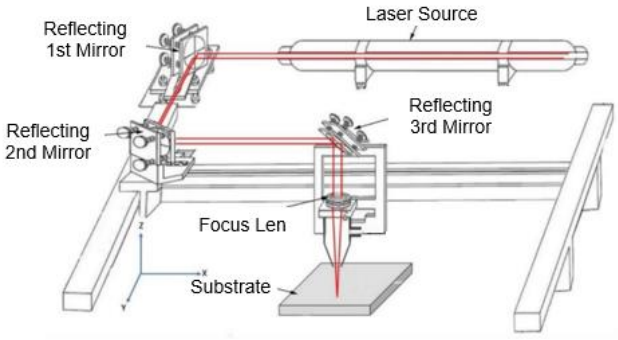

Figure 12 - Schematic of a laser CO_2 system. Adapted from [105]

4.3. Characterization Equipment

4.3.1. 4-point Probe Resistivity Measurement Device

The first step of the work was the study of the sheet resistance of samples of the LIG formed on paper with chemical treatment with and without being embedded in wax. The equipment used for this study is the Biorad *HL 5500*, presented on **Figure 13**.

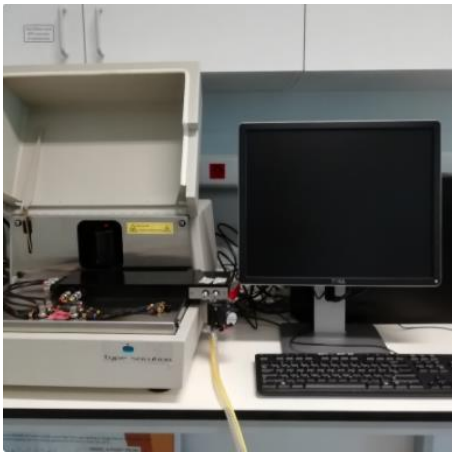

Figure 13 -Biorad HL 5500 sheet resistance equipment at CEMOP laboratory of Electrical Characterization

The most common and simplest technique for measuring the sheet resistance is the four-point probe method or Van der Pauw Method.

This method to measure the sheet resistance admits that the sample to be measured is homogeneous, isotropic, its thickness is uniform throughout all the sample and is smaller (at least one order) than its width and length, also the contacts must be the smallest possible, once the error of the measurement will be of the order of the division between the mean diameter of the contacts and the distance between the contacts [106].

The operation process of the measurement occurs though the application of an electrical current between two of the probes, and then the potential difference is measured between the other two probes. Ohm's Law states that the resistivity of the material is given by the following equation: $R = \frac{V}{I}$, where R is the resistance, V is the tension measured and I is the current applied.

Sheet Resistivity ,R_s, is an important electrical property to measure on semiconductor materials, it consists in the measure of lateral resistance per square of area of a material and quantifies the ability of electrical charge to travel in the plane of the film [107]. It is given by the following equation:

$$R_s = \frac{\pi(R_{\alpha\beta,\gamma\delta} - R_{\beta\gamma,\delta\alpha})}{2\ln(2)} f$$

Where f is the Van der Pauw correction factor, that is dependent of $R_{\alpha\beta,\gamma\delta}$ and $R_{\beta\gamma,\delta\alpha}$. $R_{\alpha\beta,\gamma\delta}$ is the resistance between the contacts αβ and γδ, when is applied current on electrodes αβ and the voltage is measured though contacts γδ and vice versa for $R_{\beta\gamma,\delta\alpha}$, **Figure 14**.

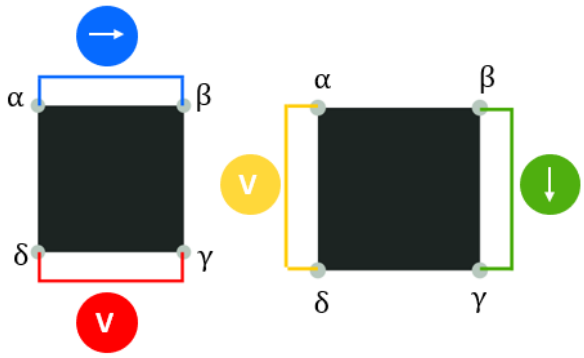

Figure 14 - Schematic the two spatial configurations of the sheet resistance measurements on a 4-point probe.

4.3.2. Scanning Electron Microscope and Energy dispersive X-ray Spectroscope

Scanning Electron Microscopy (SEM) is a non-destructive technique that informs about the morphology, topography and structure of a substrate surface forming three-dimensional black and white images. The laboratory equipment used in this dissertation was Hitachi TM 3030Plus Tabletop Microscope, **Figure 15**.

Thanks to the technique's high magnification and resolution, and high depth of field, it is very useful to detect impurities, discontinuities and texture on the material's surface [108]. SEM works only on electrically conductive materials [109].

The physical principle behind the formation of SEM images is the same as light microscope with the difference that the surface material is irradiated an electron beam formed by an electron gun accelerated by a potential difference and focused through magnetic field lenses and metal slits within vacuumed column, instead of photons at the visual spectra

(light), whose interactions cause the emission of secondary, backscattered, and diffracted backscattered electrons but also photons whose wavelength are in the infrared, X-ray, and visible spectra depending with on the interaction that occurred [109]. The image is mostly formed by secondary electrons and backscattered electrons that are captured by the detector. The secondary electrons provides the highest spatial resolution, informing about the morphology and topography of the sample surface meanwhile the backscattered electrons gives the image compositional contrast [13][14].

The Energy- dispersive X-ray Spectroscopy (EDS) equipment is commonly attached to SEM equipment [14]. The system that was used in this dissertation was Bruker Scan Generator and XFlash Min SVE. EDS is based on the detection of the X-ray photons emitted due to the electron beam interaction with atoms of greater depth on the sample [109].

The physical phenomena behind the emission of X-ray photons starts after the ionization of an electron of an inner level after interacting with the electron beam forming a gap. This gap is filled with an electron from a higher energy level resulting in the emission of X-ray photon which energy depends on the transition of the levels that is characteristic of the element [111].

This technique gives information about elemental composition surveys. This technique gives the atomic percentages of species present on the sample and its spatial presence [111].

Figure 15 - Hitachi TM 3030Plus Tabletop Microscope available at CENIMAT|i3N

4.3.3. Micro-Raman Spectroscope

Micro-Raman Spectroscopy gives information about the chemical species, molecular structures, and the conformation of the materials, as also identification of substances. This technique is known for its strong, rapid, sensitive, and non-destructive analytical approach to provide both qualitative and quantitative information [112].

When a monochromatic electromagnetic radiation interacts with the molecules on the sample inducing the formation of an electric dipole by its polarization provoking the scattering of electromagnetic radiation [112].

The scattering of radiation can be of two natures, elastic (Rayleigh scattering) or inelastic scattering (Raman Scattering). Scattering is considered inelastic when the scattered radiation has different frequency than the incident radiation. When the analyte molecule absorbs energy and the scattered radiation has lower energy, it is called a Stokes Raman scattering. When the molecule loses energy and the emitted radiation is higher than the incident radiation, the phenomenon is named Anti-Stokes scattering. The energy difference is specific of the molecule, once it depends on the mass of the nuclei and strength of the atoms [112], [113].

The Raman spectra plot contains the relative wavenumber values with the applied excitation wavelength [112].

The equipment used was Renishaw in Via Qontor Raman microscope displayed on **Figure 16**.

Figure 16- Renishaw in Vua Oontor Raman Microscope used in this dissertation available at CENIMAT|i3N

4.3.4. Potentiostat

A potentiostat is an electronic device that haves 2 main modes of operation. In the potentiostatic mode the potential of the CE is controlled to obtain a specific potential difference between the WE and RE. The galvanostatic mode, a current flow is injected between the WE and CE, while the potential difference between the WE and RE is measured [114].

In this work, the equipment used was PalmSens4 Potentiostat. It has cell cable with WE, RE, CE connectors and ground, PSTrace software for Windows. It has a large potential range from -5V to 5V or from -10V to 10V and current range from 100 pA to 10 mA [115].

Figure 17- PalmSens4 portable potentiostat [115]..

4.4. Experimental Procedure

4.4.1. Chemical Treatment of Paper and Wax Coating

Paper is a flammable material. Therefore, to occur the conversion of cellulose fibers to graphitic material we need to apply a chemical treatment with a fire retardant to the sheets of paper. This treatment avoids the ignition of the substrate by the laser irradiation [29].

The treatment consists in the submersion of an A6 chromatography paper sheet in a solution of sodium tetraborate decahydrate on 10 min each side of the sheet and left to dry [29]. Sodium tetraborate promotes the formation of a protective coating on the char inhibiting the release of combustible gases from the burning materials, also it promotes the release of chemically bonded water in sodium tetraborate decahydrate [116].

After the solution of sodium tetraborate has dried on the chromatography paper sheets, one layer of solid wax with the Xerox ColorQube wax printer is applied to the paper.

Then the paper must be placed on a hot plate for 2 minutes at 120 °C melting the wax so that it penetrates the full thickness of the paper. This process allows the impermeabilization of the substrate [29], [117].

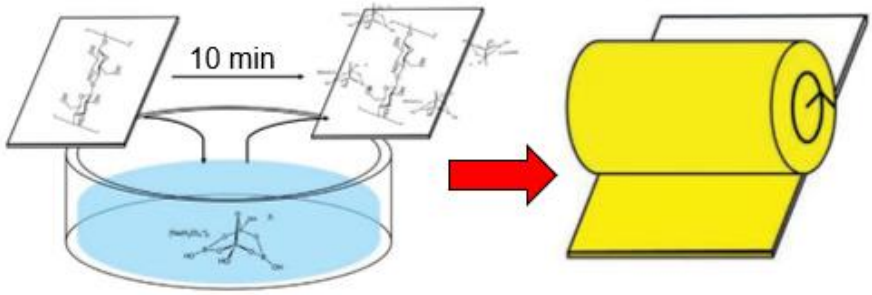

Figure 18 - Representative image of the chemical treatment of paper with sodium tetraborate followed by the paper wax coating process. Adapted from Pinheiro et al. [29]

4.4.2. Regulation of the Surface of the Paper

The chemical treatment of the paper has the side effect of increasing the surface paper roughness and adding height irregularities. Therefore, the paper sheets are fixed to a glass substrate with tape to assure the most uniform surface possible and to minimize the impact of the irregularities over the LIG formation.

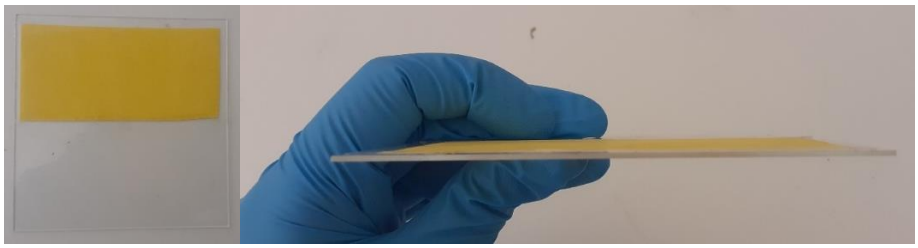

Figure 19 - Demonstration of the affixation of the treated paper on glass with tape.

4.4.3. LIG Fabrication and Optimization

The first step of this dissertation consisted of the optimization of the LIG formed on treated paper. Several types of characterizations of the LIG were performed to classify its quality. The first study centered on the characteristics of LIG on paper formed with different laser parameters of power and speed.

The environment of the chamber during the lasing process was manipulated with the insertion of nitrogen. The presence of nitrogen, an inert gas, during the lasing of the substrate helps to reduce its ablation [39]. The room temperature where the VLS 3.50 laser is inserted varied between 20 to 25 °C.

Laser Parameter Optimization Matrix

The first step of the work consisted of the production of two laser parameter optimization matrices that study the laser fabrication conditions of power and speed that result in the formation of LIG with the best electrical and chemical characteristics.

The matrix consisted of 8×8 squares each with 5mm of side varying the power and speed settings from 1 to 8% (0.50 to 4.00 W and 1.27 to 10.16 cms^{-1}, respectively) of its operating capabilities at the fixed height of $z = -2.54\ mm$, which is $0.79\ mm$ from the focal plane, that is set to $z = -1.75 mm$.

The production of both matrices started by the design of each row of squares on *Adobe Illustrator CC 2015*. The color of each square is equivalent to the laser conditions of power and speed in the laser software. On each row, with a fixed power percentage, the speed percentage varies from square to square from 1% to 8% with a 1% step. The matrix is obtained by repeating the production of the row of the square 7 times, increasing the power percentage from 1% to 8% in each row. On the first matrix, the laser irradiation of the substrate oc-

curs only once, while the second optimization matrix was produced by lasing the substrate a second time with the same combination of laser parameters.

The LIG formed was characterized firstly by observing the integrity state of the substrate, which caused on some laser parameters its ablation or weak or nonexistent LIG production.

Figure 20 - First row of the LIG optimization matrix, where each color represents a different combination of laser power and speed.

Electrical Characterization

All the conditions that produced graphitization of the substrate were electrically analyzed by the measurement of its sheet resistance. To study the reproducibility of the lasing conditions, four 5mm square LIG samples of each combination of scan passes, laser power and speed were produced. On each edge of the LIG square is placed silver ink to improve the contact with the equipment probes, as appears on **Figure 21 A).** To accelerate the process of drying of the silver ink, the samples are placed on a hotplate at 50°C for 30 minutes. The sample is then placed on the equipment with a glass underneath, and the four equally spaced probes are allocated on the edges with silver ink, **Figure 21 B)**, and the sheet measurements are made.

Structural Characterization

For the analysis of the structure of the LIG formed on the surface of the substrate, it was used the following techniques Scanning Electron Microscopy (SEM) and Energy-dispersive X-ray Spectroscopy (EDS).

The first study using this characterization used square samples with a side length of 5mm of LIG with the conditions of the power of the laser and scanning speed that give the lowest sheet resistance on waxed paper with the treatment explained in section 4.4. Each LIG samples images was examined 3 times. The images were captured with 15kV accelerating voltage and with the Mix detector, which corresponds to both scattered and backscattered electron detectors, and200×, 1500×, 3000× zoom.

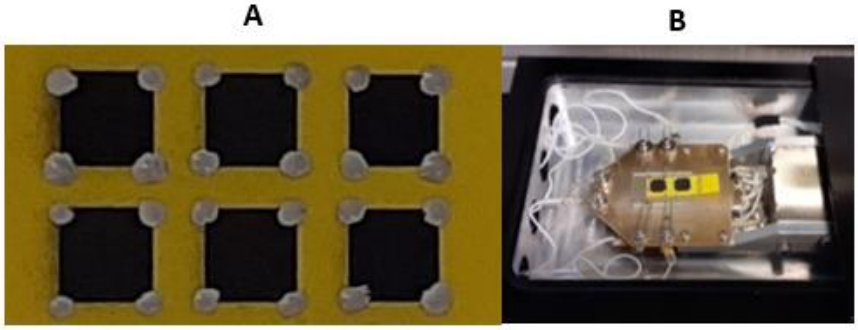

Figure 21 - **A)** Final product design to study the sheet resistance of the LIG samples. **B)** Experimental setup ready to measure the sheet resistance of one sample.

Micro-Raman Spectroscopy

Raman Spectroscopy is a technique that can be used to give information about the structure quality of the LIG produced. Each sample was measured four times with the Renishaw Centrus 2957T3 detector incorporated into the Raman spectroscopy equipment using the green laser, whose wavelength is 532 nm. 50% of laser power was used to study the LIG samples, the time of acquisition used was 10 seconds and it was performed 3 accumulations.

4.4.4. Temperature Sensor Fabrication and Testing

Temperature Sensor Fabrication

Three designs were initially proposed for the temperature sensors developed on this dissertation, **Figure 22**. The LIG thermoresistive designs are composed of two areas with different functions. Both rectangles on the extremities of the sensor correspond to the area that is going to contact the Kethley crocodiles. To enhance the electrical contact and turn this area more resistant to abrasion from the contact and be able to make several measurements with the same sensor, this area is painted with silver ink. The other area consists of the sensor sensitive area. This project consisted of LIG rectangles of different sizes.

The design in **Figure 22A)** was made with the biggest area and served as a proof of concept that LIG on paper has the physical properties to vary with temperature, and it could be used for this dissertation.

The following designs, **Figure 22 B)** and **C)** were produced with the aim of being tested on an *in vivo* rodent model. The sensor sensitive area of the sensors must be smaller than the simulated 6mm diameter ulcer provoked by a biopsy needle on the mice's back, according to the project proposal. The sensitive area of each sensor corresponds to a square with 3mm of side and 5mm of side, and the electrodes on both designs were 3mm side square.

The LIG formed on the treated paper substrate under an N_2 atmosphere were produced firstly with 2 passes of 6% of the laser power and 8% of the laser speed. Since this laser configuration was the one which showed better conductive results, from the electrical characterization step. However, this combination of laser power and speed provokes extreme laser ablation on some of the sensors produced. Alternatively, it was used 5% of laser power and 7% of laser speed, that had a good electrical response and didn't compromise the state of sensor, on the Appendix is the conversion table of laser parameters to standard units.

After the production of LIG on the treated paper substrate, the sensor is aligned with plastic laminated pouches covered with adhesive tape with openings using 80% of the laser power and 100% of the laser speed on the Vectorial Mode. Later the cut laminated pouches encapsulate the sensor after passing through a thermal laminator. The openings on the plastic pouches frame with the contact area, so the following step is painting the contacts with silver ink.

To cure the silver ink, the sensors can be left at environment temperature on a hot plate at 75ºC for 2 hours. After the silver ink on the contacts is dry, the excess of silver ink can be separated by removing the adhesive tape.

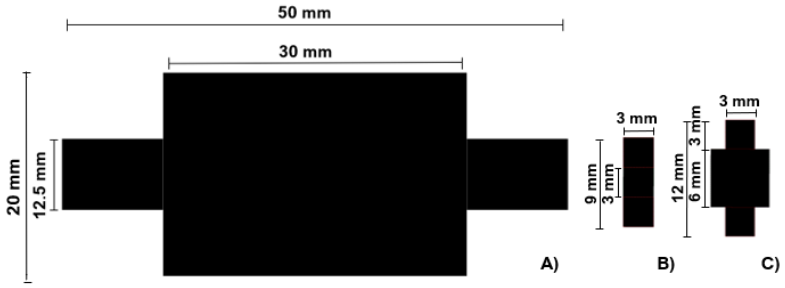

Figure 22 - Designs used for temperature sensor monitoring.

Thermoresistive Testing and Validation

The experimental setup used to characterize the behavior of the resistive sensor with the alteration of temperature is on **Figure 23**. The procedure consisted of putting the sensor on the Torrey Pines Scientific hot plate fixed with Kapton tape to a glass to regulate the surface of the paper substrate to ensure a uniform variation of temperature along the sensitive area of the sensor. Kapton is a good material to perform this function, since it supports a wide range of temperatures and will not melt.

Fixating the sensor to the glass inhibits the possibility to make direct contact between the electrode and the crocodile tips that connect to Kethley Source. So, the connection was made with adhesive copper tape and silver wire. The adhesive copper tape could be stuck to

the contacts after the silver ink is curated. While the silver wire in contrast needs to be attached with the silver ink before it is dried.

The current of charges that move on the sensor is measured while is applied difference potential between the 2 contacts between 0.1 V to 1.5V. The current vs potential measurement process is repeated for each Celsius degree of the hot plate. The temperature of the hot plate is set at 26 ºC then increased until it reaches 40 ºC with a 1 ºC step. The values of current were read on the Kethley and written manually on an Excel sheet.

Figure 23 - Experimental setup for the temperature sensor measurements.

Thermoresistive Sensor Humidity Characterization

The experimental setup used to study the resistance of the thermoresistive sensor at environmental temperature with altering humidity is on **Figure 24**.

The experimental setup is composed by a potentiostat, which WE and CE crocodile tips are connected to the contacts of resistive LIG sensor, that performs the measurement of the impedance. To obtain a closed environment the sensor and the crocodile tips of the potentiostat are placed on the chamber, that incorporates a humidity sensor to quantify the relative humidity that is linked to an Arduino that registers automatically on an excel file. The humidity of the chamber is manipulated by manually opening the nitrogen hose. And finally, the chamber is placed on a Faraday cage, to minimize the interference from external electrical fields.

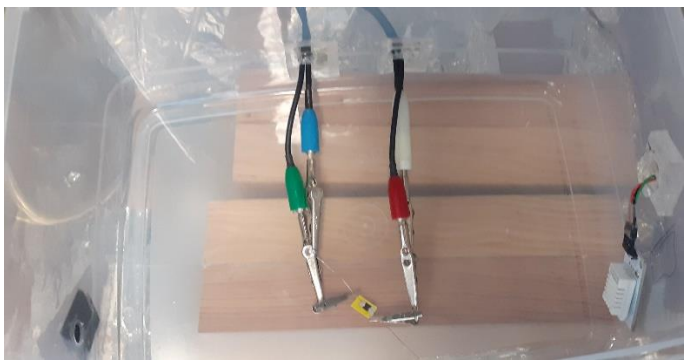

Figure 24 - Inner view of the chamber of the experimental setup of the humidity measurements.

4.4.5. pH Sensor Fabrication and Testing

pH Sensor Fabrication

The conditions of the LIG fabrication on the treated waxed paper for the development of the potentiometric pH sensor were 2 passes with the laser power at 5% and 7% of the scanning speed.

As any electrochemical sensor, the potentiometric sensor developed is composed by three electrodes RE, WE and CE as it can be seen on **Figure 25 A)**. The WE have a circular shape with 3 mm in diameter. The architecture used was designed with the program Adobe Illustrator and submitted on the VLS 3.50 laser software to irradiate the substrate with the design of interest resulting on **Figure 25 B)**.

The following procedure of the fabrication consist of cutting openings on laminating pouches with the red pattern at **Figure 25 C)**. Then sensors are aligned with each laminated pouch covered in tape, to serve as masks and sealed by passing them through a thermal laminator. The laminated pouches, as said on the fabrication procedure of the temperature sensors, gives the sensors a more robust structure and make them easier to manipulate, but also help the solutions drop-casted at the working area not pass to the contacts.

The openings allow the sensor working area and the contacts exposed once these areas are altered as you can see on **Figure 25 D)**. The contacts must be exposed once they're going to be silver painted with painting brushes. This step increases the sensor electrical conductivity and gives mechanical resistivity to this area, that will suffer mechanical stress when the crocodile tips of the potentiostat are placed. Relatively to the working area, this area is exposed for two reasons: the RE tip is painted with Ag/AgCl. Lastly the sensor working area needs to be in physical contact with the solution whose pH is of interest to the measurement. The removal of the tape of the laminated pouches confers a uniform and constant painting area, by helping us remove the excess of ink, **Figure 25 E)**.

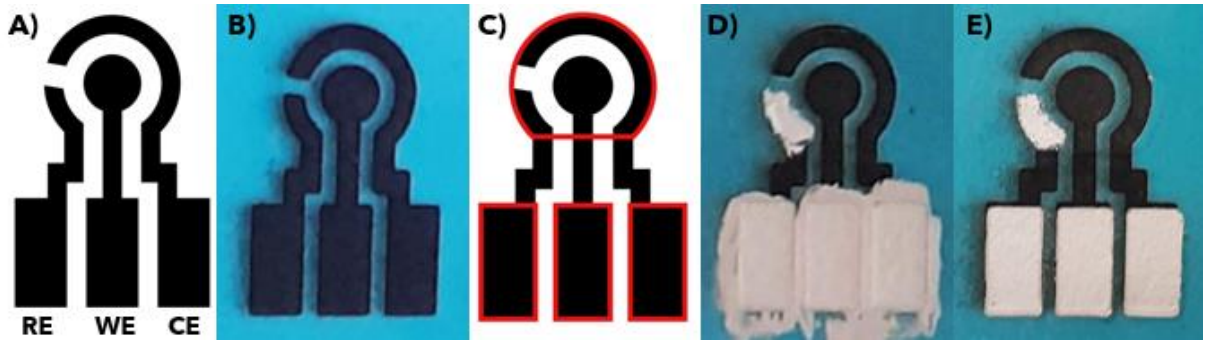

Figure 25 - pH sensor fabrication steps: **A)** design of the area that will be laser engraved on the treated and waxed paper, and identification of each sensor electrodes (RE, WE, CE), the diameter of the WE is 3 mm, the area of each electrical contacts is $2.9 \times 5.6\ mm$; **B)** LIG electrodes after laser engraving the substrate; **C)** design uploaded on the laser sofware, the black color encodes the engraving design of the sensor, while the red color encodes the shape of the openings on the laminated pouches; **D)** encapsulated sensors painted with silver ink on the contacts and Ag/AgCl ink on the RE; **E)** complete pH sensor

Modification of the Working Electrode

Then the WE was modified by electropolymerization of aniline. The cyclic voltammetry (CV) scans were made by connecting the potentiostat electrical clips to their respective silver contact, blue for the RE, red for the WE, and black for the CE, as appears in **Figure 26**.

The first step before performing the eletropolymerization the WE involved electrochemically cleaning the working area by drop-casting a 60μL solution of 0.5 M of hydrochloric acid, HCl, and executing 10 cyclic voltammetry scans within the potential interval of [-0.3, 1.1] V at a scan rate of 0.1 Vs^{-1}. After, the HCl solution is removed with paper tissue.

Then to execute the electropolymerization of PANI on the WE, it was drop-casted an 60μL solution of 0.1 M of aniline in 1M of HCl solution on the working area. Followed by 12 CV's scans from -0.2 V to 1.0 V with the same scan rate of the CV's scans used to clean the WE. Then the aniline solution on the working area is replaced by a fresh 60μL solution and the application of 12 CV's scans was repeated.

Subsequently, morphological, and chemical studies were carried out through SEM, EDS, and Raman analysis. This characterization was conducted on LIG pH sensors previously PANI electropolymerized, whose LIG laser parameters used consisted of 2 scans of 5% of the laser power and 7% of the laser speed, on the Appendix is the conversion table of the laser parameters to standard units. The SEM images were taken with 15kV of accelerating voltage with the scattered and backscattered electrons detector activated. All the SEM images of PANI electropolymerized on LIG have 200x ampliation. This analysis was complemented by the observation of the EDS images with additional information about the relative elemental composition of the samples.

Figure 26 - Demonstration of the final step of electropolymerization WE final step on the pH sensor

Production of the Britton Robbinson Buffer Solution

Solutions with different pH were produced through the Britton Robbinson (BR) buffer solution.

This buffer is made by mixing on a glass beaker on top of a magnetic stirrer with a magnet inside equal parts of 3 acids of diminishing strength, respectively boric acid, acetic

acid, and phosphoric acid, with the same molarity of 0.4 M. Then it is added sodium hydroxide solution of 1.75 M to increase the pH of the buffer solution to the pH of our interest.

Then to prepare the solutions with varied pH from 2 to 9 with a step of 1 pH level between two solutions. All the solutions were stored in Eppendorf tubes of 2 ml.

pH Sensor Testing and Validation

After the WE modification was left to desiccate overnight. The performance of the pH sensors was tested by recording an OCP with the PalmSens Potentiostat with the crocodile tips positioned on the respective electrodes and dropcasting 60μL of BR buffer solutions with different pH levels on the working area.

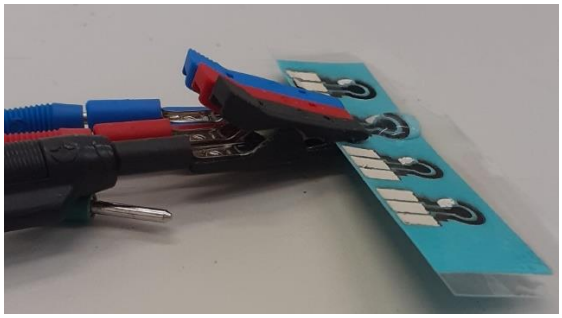

Figure 27 - Demonstration of the sensor connection on the OCP measurements.

5.

RESULTS AND DISCUSSION

The results obtained through the experimental work of this master dissertation are presented and discussed in this chapter. This chapter includes the optimization of the fabrication of paper LIG, followed by the fabrication of the temperature and pH sensors.

5.1. Laser Parameter Optimization for LIG Fabrication

LIG fabrication optimization started with the study of the influence of the laser power and scanning speed with one laser scan and two laser scans with the same combination of power and speed as the first laser scan respectively. Electrical, chemical, and morphological characterization was performed to study the effects the laser production parameters and the number of scans had on the LIG produced. The electrical characterization of the LIG formed was made through sheet resistance measurements on the samples that lead to graphitization. The samples that demonstrated better electrical performance were morphologically characterized by SEM, EDS, and Micro-Raman Spectroscopy.

5.1.1. Laser Power and Scanning Speed

Single Laser Scan

The first step of the LIG optimization consisted of the study of the conditions that allowed the formation of LIG on the waxed paper surface. **Figure 28** is the resulting matrix of the power and speed of the laser presented in the section 0, where each parameter varied it's range percentage from 1% to 8% (0.50 to 4.00 W and 1.27 to 10.16 cms^{-1}, respectively) at the laser platform height of $-2.54\ mm$. Through an analysis of the matrix, it is possible to divide the laser irradiation conditions into 3 groups. The conditions that cause ablation of the substrate, conditions that allow the formation of graphene, and lastly the conditions that do not cause any effect on the substrate.

The first group occurred when the scanning speed percentage is lower than the power percentage. In these conditions, the substrate absorbs large amounts of energy breaking all the chemical bonds and provoking ablation and perforation of the paper.

The second group occurred when the percentage of the speed of the laser capabilities was equal to or higher than the percentage of the power of the laser. These conditions allow the formation of graphene in the substrate once the energy absorbed is sufficient to break the C-O, C=O and C-N bonds.

In the third group, for scanning speed percentages that are higher than the power percentage, the energy absorbed by the substrate is not enough for LIG formation.

To sum up, LIG formation only occurs when the energy absorbed by the substrate is high enough to break chemical bonds allowing the lattice recombination without causing ablation of the substrate.

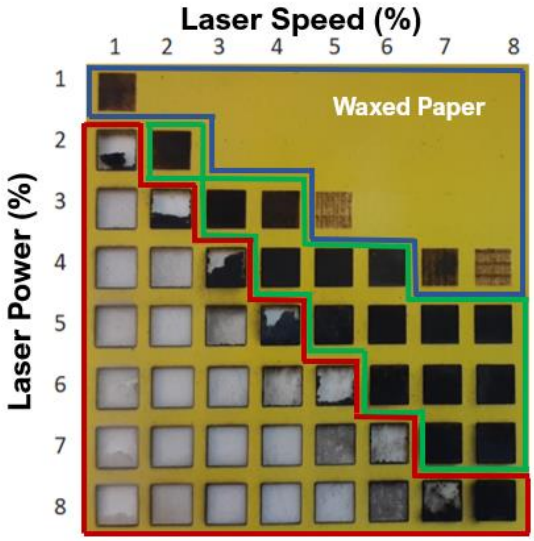

Figure 28 - Resulting Matrix of the paper LIG formed by combination of the laser power and scanning speed. The area limited by the green line corresponds to the fabrication conditions that provoked the formation of LIG. The area circumscribed by the red line contains the laser conditions that resulted in the ablation of the substrate due to the high irradiation energy. Lastly the area delineated by the blue line, encloses the conditions whose irradiation energy did not induce LIG formation on the substrate.

Multiple Laser Scanning Influence Study

The study of the influence that multiple laser scans had on the LIG formed was performed assuming that this modification would enhance LIG electrical properties by increasing the graphene induction on the substrate [41]. The graphene formation mechanism suggested that on the first laser exposure the carbon precursor is converted into an amorphous carbon and only on the following laser exposures the amorphous carbon is converted into graphene. Suffering an increase in electrical conductivity [39], [41].

Multiple laser scan influence on the LIG quality was studied by the production of LIG samples fabricated with 2 laser scans with conditions that didn't lead to substrate ablation on the first laser scan.

5.1.2. Electrical Characterization

Afterwards, 4-point Probe resistivity measurements were performed to obtain the electrical characterization of LIG samples that showed possible LIG formation produced with 1 laser scan on treated paper, 1 laser scan on waxed printed treated paper, and 2 laser scans on waxed printed treated paper. The sheet resistance results appear on **Figure 29**.

For the analysis of the influence of the wax printing stage on LIG fabrication, one laser scan treated paper LIG samples with and without the wax printing process were electrically studied, as it can be seen by the blue and yellow bars on **Figure 29**. The majority of LIG samples on waxed paper produced under the same fabrication conditions than the LIG produced on treated paper had smaller sheet resistance, leading to the formation of more conductive LIG. Paper samples with wax have less spatial distance between the cellulose fibers, once the melted wax occupies the space between the fibers, constructing a smoother substrate surface that could lead to homogeneous graphitization. Also, it was observed that conditions that lead to extreme ablation on LIG treated paper samples demonstrated less ablation on LIG waxed treated paper samples. A possible justification could be that wax may contribute to the inhibition of substrate combustion.

Additionally, the study of the LIG electrical performance dependency relatively to multiple scans on waxed paper was done by the comparison of the sheet resistance values of waxed paper LIG samples produced with the same set of laser power and speed with one laser scan represented by the yellow bar, and two laser scans, depicted by the orange bars on **Figure 29**. After the second laser scan the number of measurable LIG samples decreases due to substrate ablation. LIG samples with two laser scans demonstrate to have a significantly better electrical performance, as expected. An example of this phenomenon is the LIG production combination of 6% of the laser power and 8% of the laser scanning speed with one single laser scan has the sheet resistance of $39.2\ \Omega/sq$ with $7.7\ \Omega/sq$ of standard deviation. While, with two laser scans this condition obtains the best electrical performance, by obtaining the lowest sheet resistance value of $16.2\ \Omega/sq$ with $2.1\ \Omega/sq$ of standard deviation.

The laser conditions not represented on **Figure 29** are the ones that did not lead to the graphitization of the substrate, or the energy of the laser irradiation induce the substrate ablation, and also the conditions that produced an excessively porous LIG were not included.

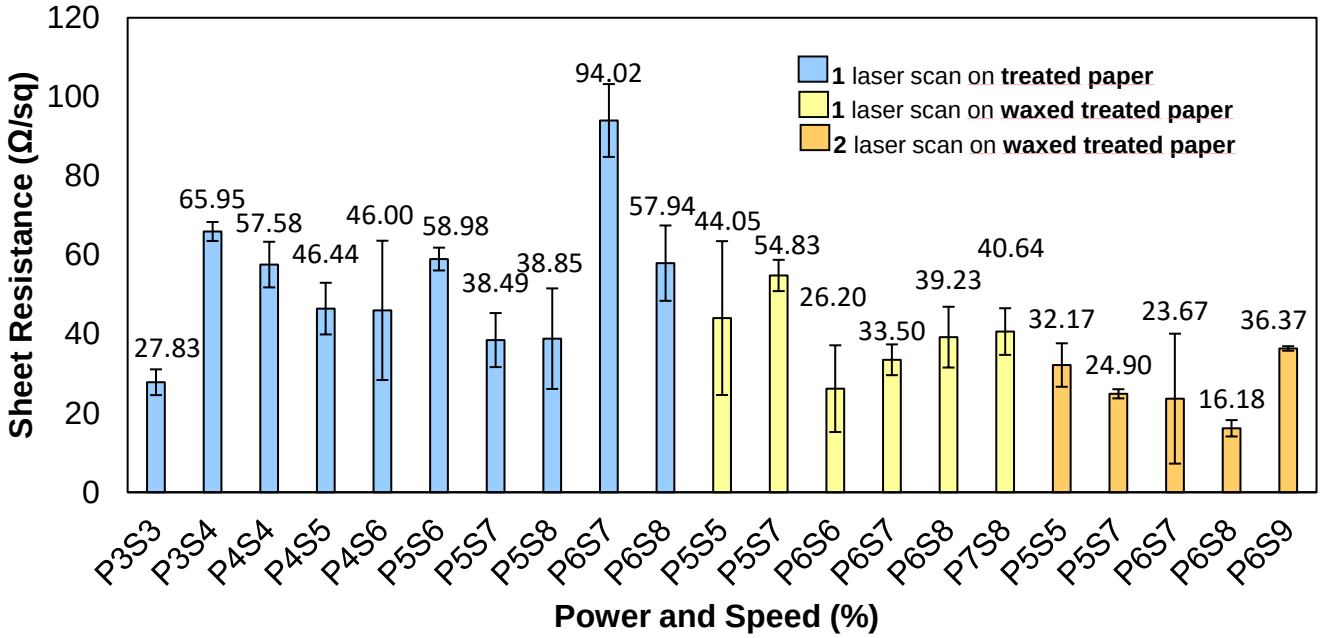

Figure 29 - Sheet resistance measurement.

The study of the LIG production parameters on waxed and unwaxed treated chromatography paper was enriching, once it was possible to obtain highly conductive LIG, with lower sheet resistance than chromatography paper-LIG presented in published recent articles, in **Table 1**.

Table 1 - Literature Sheet Resistance for LIG produced in chromatography paper.

Sheet Resistance Ω/sq	References
132.00	[93]
61.50	[118]
56.00	[119]
~40.00	[120]
32.00	[30]
16.18	LIG on waxed chromatography paper in this work

5.1.3. LIG Morphological, Chemical and Structural Characterization

The consequences of the paper laser irradiation were observed, quantified, and analyzed making use of the morphological, chemical, and structural techniques of SEM, EDS, and Raman. In the first place, SEM images were studied. This technique allowed the analysis of the morphology of the surface of samples and see the effect that laser irradiation had on cellulose fibers of the substrate. **Figure 30 A**) consists of the resulting SEM image with a

magnification of chromatography paper after the fire-retardant treatment with sodium tetraborate with no laser irradiation. As can be seen, it is possible to discern with clarity the paper fibers. Then it produced a SEM image with the same magnification as the previous image of the same substrate, however, irradiated with 2 laser scans with 5% of its operational power and 7% of the scanning speed. After the laser irradiation the paper fibers cannot be seen with clarity, all we see it's an irregular and porous surface, because of the gas liberation induced after the bonding breaking of carbon atoms presented on the cellulose fibers with the oxygen and other elements, which indicates the formation of LIG, a 3D foam like porous graphitic structure **Figure 30 B)**.

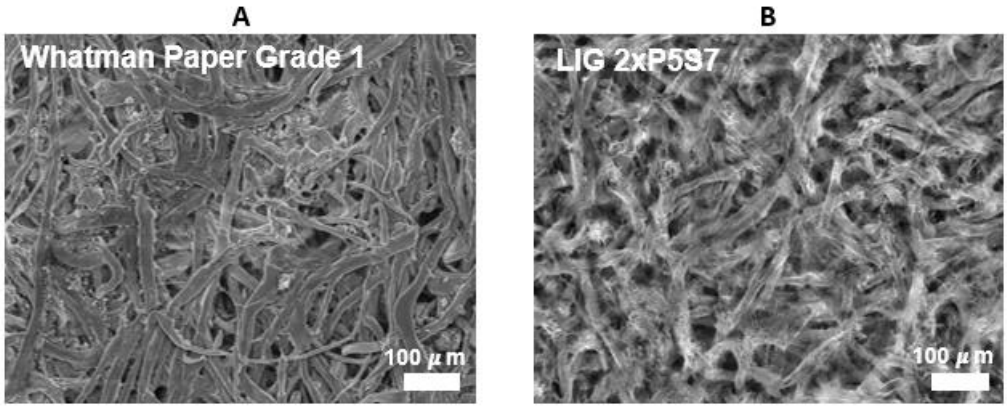

Figure 30 - SEM images of A) pre-treated paper without laser irradiation B) paper after 2 scans with 5% of the laser power and 7% of the laser speed.

In the second place, the EDS technique gives information about the relative chemical composition of the surface of the sample confirming the morphological changes observed with the SEM images. The samples used for this characterization were LIG squares with 6mm of side length with 2 laser scans of 5% of the operational power of the laser and 7% of its scanning speed. The EDS map of the LIG area, **Figure 31 B)** has an elevated distribution of blue color in comparison with the treated paper area, **Figure 31 A)**, meaning a higher concentration of carbon (C) on the area. Analyzing the atomic percentages in **Figure 31 D)**, it is possible to conclude that the main constituents on both EDS maps are carbon and oxygen (O). The presence of sodium (Na) in both areas is due to the fire-retardant chemical treatment with sodium tetraborate. The paper area not irradiated has a lower average percentage of carbon 51.4% with 2.9% of standard deviation between the 4 samples, and a higher percentage of oxygen 46.4 % with 1.8 % of standard deviation, and sodium 2.2% with 0.7% of standard deviation, compared with the sample irradiated. Additionally, the ratio between the percentage of carbon and oxygen in the substrate area with no laser irradiation is a similar to the ratio that these elements appear in the cellulose chemical formula, as you can see in **Figure 31 C)**. The relation between the atomic percentages of carbon, oxygen, and sodium in both areas can be explained by the phenomenon of laser irradiation on the substrate, as said

in section 2.2. When the energy of the laser is sufficient to break the bonds C-O, occurs the liberation of the elements O and Na in its gaseous form, subsequently diminishing the average relative atomic percentage to 10.0% with 1.4 % of standard deviation and 0.7% with 0.2% of standard deviation on 4 samples respectively of each element. This phenomena is followed by the formation C-C bonds between the carbon atoms left in the matrix causing an increase of the average carbon percentage, 89.3% with 1.1 % of standard deviation on 4 samples.

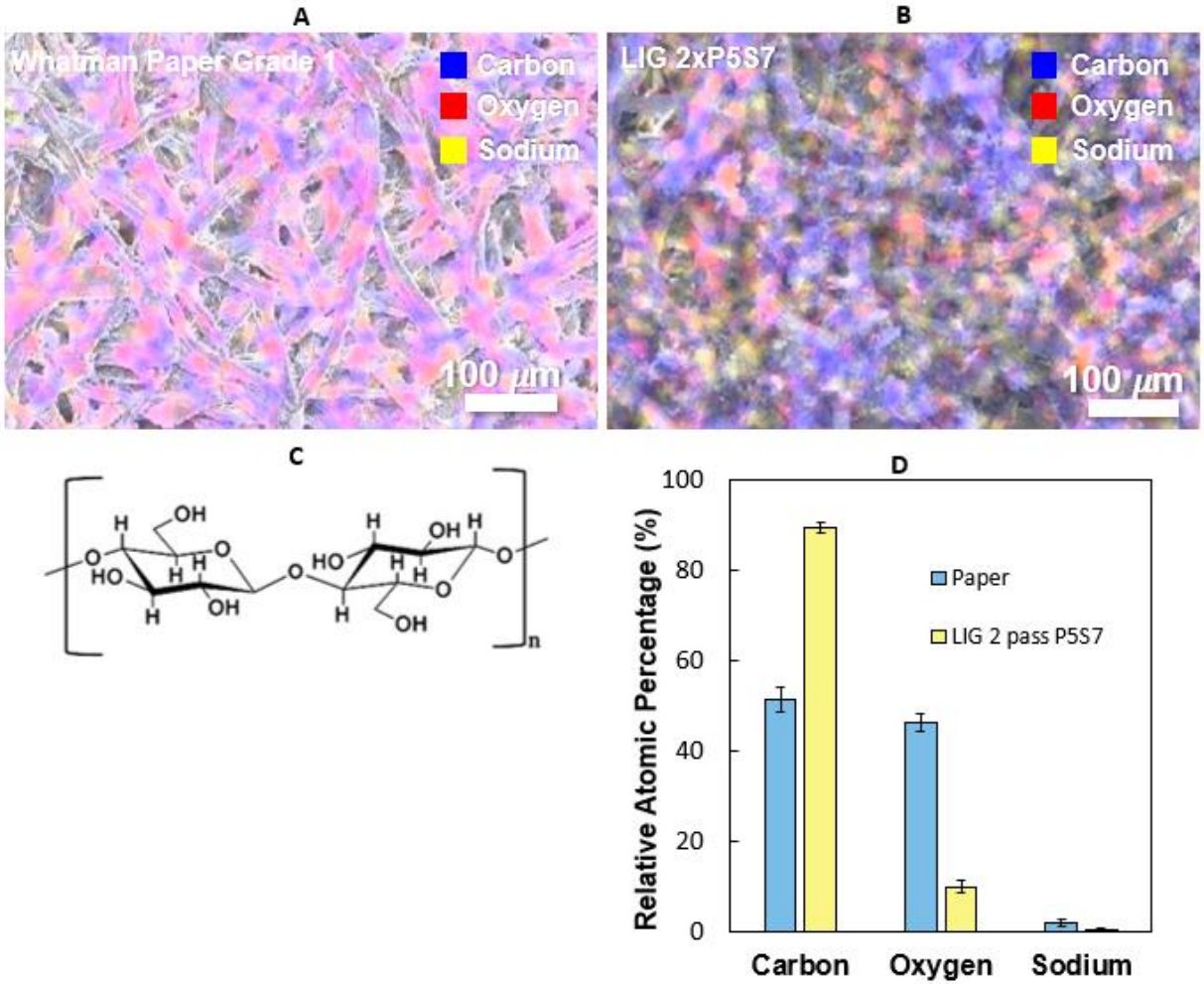

Figure 31 - **A)** EDS map of pretreated paper and **B)** EDS map of paper fibers after 2 laser scans with 5% of the laser power and 7% of the laser speed. **C)** Chemical Formula of cellulose adapted from Vicente Neto **D)** Relative atomic percentage of carbon, oxygen, and sodium.

In the third place, Raman Spectroscopy was used to investigate the graphene structure and number of graphene layers [108]. According to literature, the Raman spectrum of graphene has 3 predominant peaks, the D peak, the G peak, and the 2D or G' peak, and they are usually found in the following wavenumbers intervals, respectively, $[1320, 1350]\ cm^{-1}$, $[1580, 1605]\ cm^{-1}$, $[2640, 2680]\ cm^{-1}$ [112]. It can also have 2 less intense peaks, the T+D peak, and the D+G peak, that are present in polymer-derived carbon materials [121]. The D

peak is related to the disorders and defects in sp^2 bonded atoms. The G peak corresponds to lattice vibrational modes (E_{2g} symmetry). The 2D peaks originates from a 2^{nd} order Raman scattering which involves two phonons near the Dirac point. The G and 2D peaks are related to the two-dimensional hexagonal lattice [112][108], [112].

The number of layers on a graphene sample is measured by analyzing the position of the 2D peak and the ratio of the peaks 2D and G, I_{2D}/I_G [108]. When the sample presents a monolayer of graphene the 2D peak is normally found at $2679\ cm^{-1}$. Also, the 2D peak of multilayer graphene has lower intensity, is broader and has a higher wavenumber. Additionally, when the number of layers increases, the intensity of the G peak increases. Consequently the ratio I_{2D}/I_G decreases with graphene layers [112].

The ratio I_D/I_G is directly proportional to the disorder present within the graphene structure. Subsequently, this ratio is useful to analyze the quality of the graphene formed on a substrate [108].

Figure 32, corresponds to the most LIG representative Raman spectra obtained with a sample produced with one single laser scan of 7% of power and 8% of scanning speed of the CO_2 laser on waxed paper with chemical treatment, on Appendix is presented the conversion table of the laser parameters to its standard units. Wavenumbers of the three predominant peaks are the following: D peak is at $1346\ cm^{-1}$, the G peak is at $1573\ cm^{-1}$, and the 2D peak is at $2677\ cm^{-1}$. Additionally, the position of the two peaks with smaller intensity that appear surrounding of the 2D peak are, the peak T+D and the peak D+G are $2445\ cm^{-1}$ and $3037\ cm^{-1}$, respectively. The ratios of the intensities between the principal peaks on graphene obtained are 0.74 to I_{2D}/I_G ratio, which demonstrates the multilayer morphology of the LIG formed and the for the ratio I_D/I_G is 0.64 indicating a reasonable defect prevalence on the LIG structure.

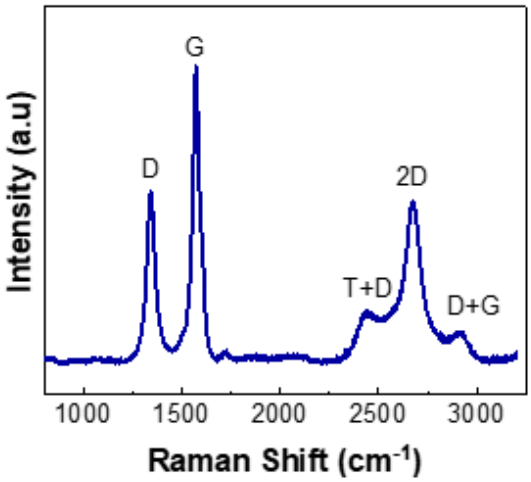

Figure 32 - Raman spectra of paper LIG fabricated with one single laser scan of 7% of the laser power and 8% of the laser scanning speed.

5.2. LIG-Based Temperature Sensor

After optimizing LIG production on paper, LDW was used to develop temperature sensors. The study of the quality of the LIG produced at different parameters of power and speed of the laser and multiple scanning was crucial to choose which conditions were the best to apply to LIG temperature sensors on paper. During the progression of the study, some alterations were made to the temperature sensors, namely adjusting the contacts to the experimental setup but also considering the project's progression, as will be shown in the following sections.

5.2.1. Temperature Sensor

The proposed sensor explored the electrical resistance to measure the variation of temperature. The measurement of resistance at each temperature was made indirectly using the Ohm's Law given by $R = \frac{V}{I}$ by measuring the current, I, while applying potential difference on a specific interval. The first temperature sensors developed, **Figure 33 A)**, had the design presented previously in **Figure 22A)**. The contact between the electrodes and the crocodile tips that connect to the Kethley Source was made with copper adhesive tape, as can be seen in **Figure 33 B)**. The conditions used to produce the temperature LIG sensors were 2 laser scans with 6% of the laser operational power and 8% of the scanning speed.

The constraints associated with this sensor were the following enumerated. The combination of design and LIG production conditions used was neither time efficient, nor environmentally sustainable, as each sensor required approximately 22-minute LIG production. Relatively the copper adhesive tape, on one hand, had the advantage that it requires no previous preparation of the sensor beyond the cure of the silver ink before the measurement. On the other hand, this material didn't guarantee a constant, durable, and homogeneous connection between the crocodile tips and the sensor, being able to alter its adhesion while the measurement wasn't finished. Another situation that occurred that turned the measurement impossible was the mechanical tension applied by the crocodile tips on the copper adhesive tape tear of the electrical contact underneath as appears in **Figure 33 C)**. This LIG production condition showed the lowest sheet resistivity. However, this condition led to deep ablation of the substrate, increasing the fragility of the sensor, and leading to unreliable and unstable current measurements.

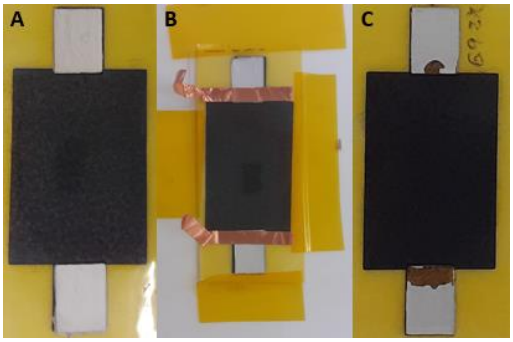

Figure 33 - **A)** Fabrication final sensor product of the first temperature sensor developed. **B)** Temperature sensor fixated to the glass substrate with Kapton tape and copper adhseive tape layout on the contacts. **C)** Temperature sensor with the electrical contact area ruptured by the mechanical tension applied by the crocodile tips of the measurement unit.

Although the combination of these limitations turned the measurement procedure very unstable, the measurement of one sample of the sensor, indicated that LIG temperature resistive sensor on paper could be a promising technique, and some improvements to LIG formed, contacts and design must be made.

Figure 34 corresponds to this temperature sensor performance. The electrical characterization was performed with increasing temperatures from 26 °C to 40°C. **Figure 34 A)** demonstrates that LIG on paper has linear I-V curves, that increase its slope with temperature. While increments of temperature provoke increases of charge particle movement trough the sensor, under the effect of a potential difference. **Figure 34 B)** corresponds to the evolution of the sensor resistance with increasing temperature. The graph shows a highly linear decrease of resistance with the increasing temperature values, with 0.982 r square. The structure of LIG is composed of disordered graphene particles forming the entire sensor's active layer. Therefore, the effect of the scattering on defects, impurities and multilayer structures have more influence on the materials behavior with temperature than electron-phonon scattering. And as the temperature increases, there is an increase of the probability of transfer of charge carriers from the valence band to the conduction band which leads to an increased conductivity and consequently reduced resistance, acting as a semiconductor [90], [91], [122], [123]. The graph on **Figure 34 C)** corresponds to the relative resistance variations as a function of the temperature variation. The curve presents a good fit with linear regression, with an r-square of 0.975. With a high sensitivity that corresponds to -1.49%°C^{-1}.

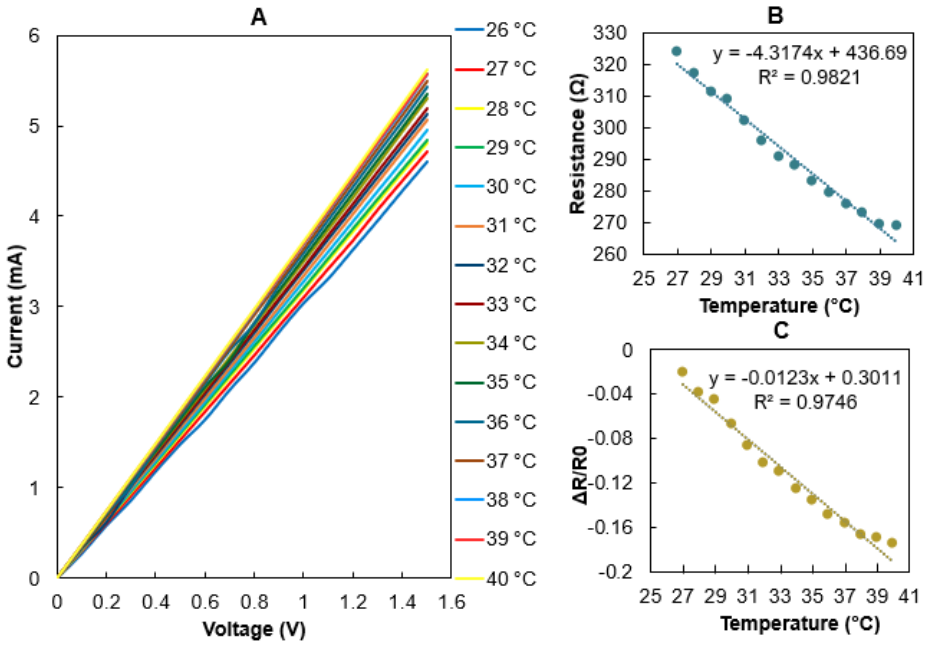

Figure 34 - Electrical characterization of the first temperature sensor design **A)** I-V curves of the sensor from 26°C to 40°C. **B)** Temperature dependent resistant of the LIG sensor **C)** Relative resistance variations of the temperature sensor from 26°C to 40°C.

Improving the Performance of LIG Thermoresistive Sensors

To improve the sensor durability, adjust it to the future work plan and upgrade the connection with the experimental setup, improvements were made to LIG production conditions, designs, along with the replacement of the adhesive tape of copper by silver wires. The new temperature sensors developed were produced with 2 laser scans with 5% of the laser power and 7% of the scanning speed. Two optimized sensors **Figure 35A)** and **B)** were developed with the designs previously presented in the section 0. These sensors were produced with the objective of diminishing the sensor area to a size that would not only allow the production of a larger number of sensors in less time while spending less electrical power but also enabled testing the sensor functionality on *in vivo* rodent models. As mentioned, rather than using copper adhesive tape, silver wires were used to improve the connection between the sensor contacts and the crocodile tips of the Kethley source-measurement unit, as appears in **Figure 35C)**. In comparison with copper adhesive tape, silver wires permitted a more stable and reliable measurement process, once its adhesion to the electrode was sturdier.

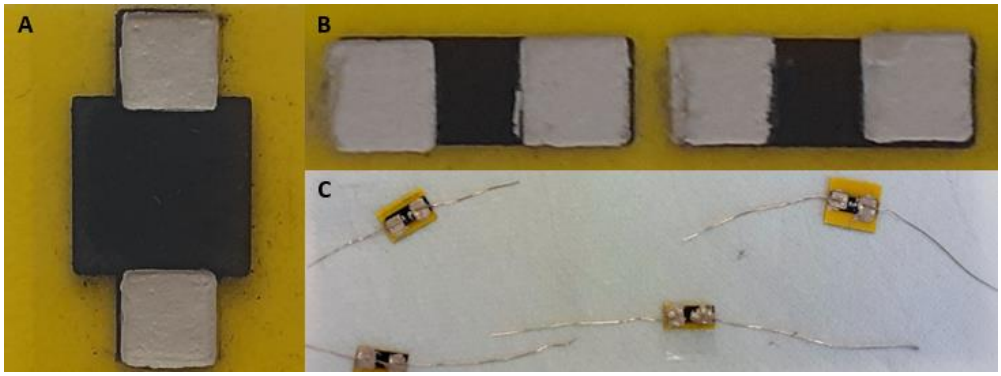

Figure 35 - **A)** Final fabrication sensor with 5mm square sensitive area. **B)** Final fabrication sensor with 3 mm square sensitive area. **C)** 3mm sensitive area sensor curing procedure with silver wires on the silver ink.

The graphs in **Figure 36** are the study that resulted from the electrical measurement of the resistance of 6 samples of the optimized sensors while varying the temperature. The graph in **Figure 36 A)** corresponds to the variation of the sensor's resistance as a function of temperature on each sample of both sensors. The curves that appear in **Figure 36 C**) illustrate the evolution of the relative resistance variation on each sample of both sensors. While the graphs on **Figure 36 B)** and **D)** correspond to the average resistance variation and relative resistance variation of both sensors, respectively.

The design of the sensors plays an important role in the electrical performance of the sensors. The longer the distance between the electrodes, the greater the resistance, since more collisions occur while the electrons travel from one electrode to the other [124]. Also, it should be considered that the bigger the cross section of the LIG sensor between the electrodes the lower the resistance since the electrons have a larger area to flow, creating more pathways for the electrons to pass and collide less [124]. Through the analysis of the graphs in **Figure 36 A)** and **C)** it is possible to make a comparison of the electrical performance of the optimized sensors. Not only did the optimized sensors with a bigger sensitive area demonstrated to be more resistive, as expected, but also exhibited a higher sensitivity to temperature variation. The sensors developed with the 3mm side square sensitive at the same temperature have very different resistance values at room temperature with a relative standard deviation (RSD) of 15% and relative variation of resistance with a RSD of 35%. The difference observed in the resistance values at the same temperature could be related to sample encapsulation didn't isolate the sensor effectively, so the resistive response of the sensor is affected by the environment humidity. While the impairment of the sensor's electrical behavior could be related to the relative humidity of the chamber when LIG production occurred. The red and yellow samples were measured on the same day but produced on different days, explaining the proximity of the resistance values and the different relative variations of resistance, once both sensors were measured under the same environmental relative humidity, but once the relative humidity on the fabrication chamber was distinct, it provoked the variation of the electrical properties of the LIG produced. The orange and pink samples were pro-

duced on the same day and measured on different days, resulting in a significant difference in the sensor resistance values, but very similar relative resistance variation. The effect of relative humidity on LIG on the paper resistive sensor is further explored in the following section.

The relative resistance variation of the optimized sensors is presented in **Figure 36 D),** both sensors show a highly linear decreasing curve, with an r-square coefficient of 0.996 and 0.992, and sensitivity of is 0.24 % $°C^{-1}$ and 0.71 % $°C^{-1}$, respectively for the 3mm side square sensitive area and the 5mm side square.

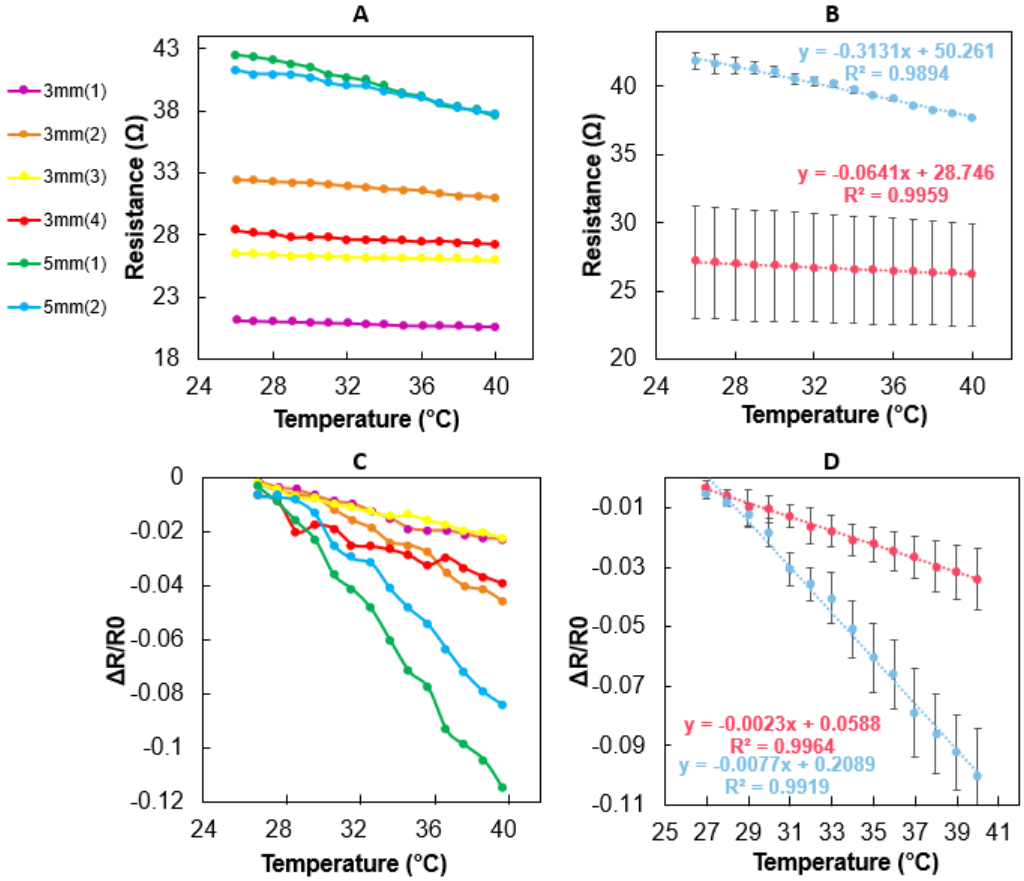

Figure 36 -Electrical performance of the optimized thermoresistive sensors. The curves on the graphs **A)** and **C)** have the following color code. The green and blue curve are two samples of the optimized sensor with bigger area, both samples were produced and measured on different days. The orange, red, yellow, and pink curves are samples of the sensor with 3 mm square sensitive area. Most samples were measured and produced on different days, except for the red and yellow curve that were produced on the same day. While on the graphs **B)** and **D)** the light blue curve corresponds to the optimized sensor with the bigger sensitive area and the light pink curve represents the optimized sensor with 3 mm square sensitive area. **A)** Electrical resistance sensors performance at increasing temperatures at each sensor sample. **B)** Resistance variation with increasing temperature of the thermoresistive optimized sensors. **C)** Relative resistance variation of the thermoresistive optimized sensors on each sensor sample. **D)** Relative resistance variation of the optimized sensors.

Testing the Resistance of the Thermoresistive Sensor with Humidity

After analyzing the resistive data measured using multiple replicas of the optimized thermoresistive sensor represented in **Figure 35 B)**, and identifying several discrepancies in the resistance variance values of sensors produced on different days, it was decided to study the sensor's electrical behavior at different humidity, with and without the encapsulation fabrication phase.

LIG on paper is a porous, fibrous, and conductive structure that turns material sensitive to electrical changes with the variation of humidity [93]. Additionally, graphene has been demonstrated to be sensitive to humidity, due to the number of oxygen groups on its surface that interact with water molecules. A solution to reduce the effect of humidity is sensor encapsulation. After analyzing the resistance interval of temperature variance discrepancy of the optimized thermoresistive sensor with a 3mm square sensitive area measured and produced on different days, it was decided to study its electrical behavior at different humidity, with and without the encapsulation fabrication phase to verify its efficiency.

The equipment used to observe the sensor resistance variation by altering the humidity was described in detail in section 0. The experimental procedure commences by measuring the resistance of the sensor at the environment humidity waiting for the sensor to stabilize its response. Then the nitrogen font is open altering the relative humidity of the chamber by incrementally introducing nitrogen gas to the chamber. Later the nitrogen source is closed, and the air surrounding the chamber starts to enter, removing the nitrogen gas, and altering the humidity of the chamber.

The curves on **Figure 37A)** and **B)** illustrate the response resistance variation of the thermoresistive sensors at environment temperature when manipulating the chamber relative humidity with the procedure previously explained. On one hand, when augmenting the environment humidity, paper LIG absorbs the moisture in the environment and swells the cellulose fibers provoking the separation of the conductive elements on the substrate and reducing the material's conductivity. On the other hand, when the humidity decreases paper LIG liberates the moisture, reducing the space between the cellulose fibers by desorption and bringing the conductive elements closer, reducing their resistance [93][125].

The variation observed on the encapsulated sensor on **Figure 37 A)** is significant. It indicates that the encapsulation process didn't effectively ensure the isolation of the sensing material being susceptible to the environment humidity. Once the electrical properties of the sensors vary with temperature and humidity, the resistive sensor must be studied considering both parameters together.

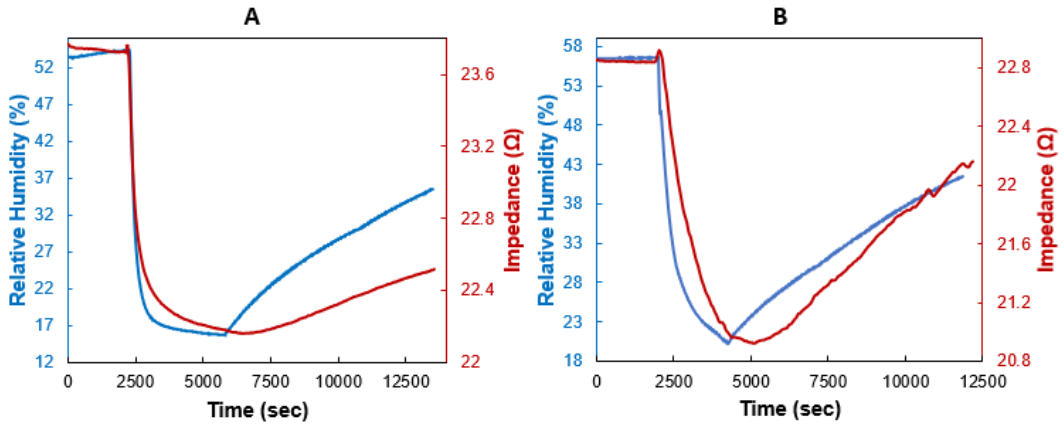

Figure 37 - **A)** Resistance of the encpasulated thermoresistive sensor (blue curve) in response to different relative humidity conditions measured on the chamber (red curve). **B)** Resistance of non encapsulated thermoresistive sensor (blue curve) in response to different relative humidity conditions measured on the chamber (red curve)

Comparison of the Thermoresistive Sensors Developed

By comparing the sensor performance of the sensors developed in this dissertation with the sensors reported in published articles, whose sensing properties are summarized in **Table 2** it is possible to conclude that the temperature sensors developed in this dissertation have a similar performance. The sensors with the biggest sensitive area have a very high sensitivity inserted between the graphene nanoribbons (GNR) sensor on PI developed by [67] and the reduced graphene oxide (rGO) sensor on PI, [92]. The sensor with the smallest area had congruent sensitivities to the LIG on paper sensor developed by [93] and the graphene sensors fabricated from plasma (Gpl) [90]. And the sensor with a square sensitive area of 5mm in size had similar sensitivity to the graphene nanoplatelets sensor (Gnp) and the reduced graphene oxide sensor on gold electrodes [90]. As can be seen, the sensors developed in this dissertation using the LIG technique produced have a negative temperature resistance coefficient, such as most of the reported ones, having a semiconductor behavior. In contrast, the graphene sensor fabricated using chemical vapor deposition (CVD) has a positive temperature resistance coefficient characteristic of semimetal materials. As a result of the material structure that this fabrication method in comparison with the other techniques develops fewer defects, decreasing the electron-phonon scattering effect [90]. In conclusion, the sensors produced in this dissertation demonstrated to be as sensitive as temperature sensors fabricated with more complex fabrication techniques of graphene with higher cost and not degradable substrates, such as chemical vapor deposition, graphene nanoplatelets, graphene fabricated from plasma and graphene reduced oxide, demonstrating the great potential that this fabricating technique has for the development of thermoresistive sensors.

Table 2 - Comparison of the sensitivity, resistance at room temperature and linearity of thermoresistive sensor produced with different fabrication techniques with graphene on different substrates.

Sensitive Material	Substrate	Sensitivity	Range (℃)	R_0 (Ω)	R^2	Reference
CVD	-	$0.265\%℃^{-1}$	[10,100]	~18	-	[90]
LIG	PI	$-0.04145\%℃^{-1}$	[30,40]	7.105	-	[91]
LIG	PI	$-0.142\%℃^{-1}$	[−10,60]	2.0×10^5	0.999	[94]
Gpl	-	$-0.168\%℃^{-1}$	[10,100]	$\sim 1.85 \times 10^4$	-	[90]
LIG	Whatman paper	$-0.24\%℃^{-1}$	[26,45]	27.11	0.9964	Sensor with the smallest area
LIG	Paper	$-0.28\%℃^{-1}$	[10,60]	~395	0.99	[93]
rGO	Au	$-0.486\%℃^{-1}$	[10,100]	$\sim 2.8 \times 10^3$	-	[90]
Gnp	Au	$-0.516\%℃^{-1}$	[10,100]	$\sim 1.4 \times 10^4$	-	[90]
LIG	Whatman paper	$-0.71\%℃^{-1}$	[26,45]	41.84	0.992	Sensor with 5mm of size
GNR	Paper	$-1.27\%℃^{-1}$	[30,80]	-	-	[67]
LIG	Whatman paper	$-1.49\%℃^{-1}$	[26,45]	323.81	0.975	Sensor with the biggest Area
rGO	PI	$-1.56\%℃^{-1}$	[25,45]	-	-	[92]

5.3. Development of pH the Sensor

Researchers have been highly interested in developing electrochemical sensors using graphene, due to its high electrical conductivity, high mechanical stiffness, and thermal conductivity. LIG is a scalable, simple, and low-cost manufacturing technique that fills up some of the limitations presented by conventional graphene fabrication methods [126], [127]. This work studies the production feasibility of PANI electrochemical potentiometric pH sensors using the LIG technique on paper, a very economical and sustainable substrate for monitoring the DFU healing state.

The pH sensors were fabricated using the production settings that were used on the optimized temperature sensors, respectively, 2 laser scans of 5% of the laser power and 7% of the scanning speed with the platform height $z = -2.54\ mm$.

The production procedure used for the fabrication of the pH sensors as described in section 0. As already stated, the WE are PANI electropolymerized. PANI is a conductive polymer used in previous studies for the development of solid-state highly sensitive pH sensors with environmental stability, controllable electrical conductivity, and reversible redox chemis-

try. PANI additionally is a low cost, biocompatible reproducible material with diverse and simple production techniques [73], [99], [128], [129].

PANI is the oxidative polymeric product of aniline [128]. The synthesis technique used in the dissertation consisted of electrochemical polymerization via CV. This technique provides a direct deposition of PANI on the electrode surface, giving the user control of the morphology and thickness of the PANI formed through the manipulation of deposition parameters [130].

The structure of PANI is a combination of oxidized and reduced units, specifically quinoid rings and benzene rings [130]. Additionally, PANI forms can also be divided into salts (protonated) and bases (unprotonated) [130]. Depending on the PANI oxidation state and the ratio between the reduced and oxidized units there is the formation of three PANI stable oxidation forms, leucoemeraldine, emeraldine, and pernigraniline [129], [130]. Emeraldine salt corresponds to the most conductive form of PANI, and it is obtained by protonation of emeraldine base [128]. This PANI form transition is the base principle used to monitor pH [99].

PANI, as an electrochromic material, suffers color changes when subjected to an electric field that induces its oxidation or reduction. When the PANI formed corresponds to emeraldine salt the WE acquire a green characteristic color. After the electropolymerization a dark green color can be observed in the WE, which suggests the presence of emeraldine salt [130], as can be seen in **Figure 38**.

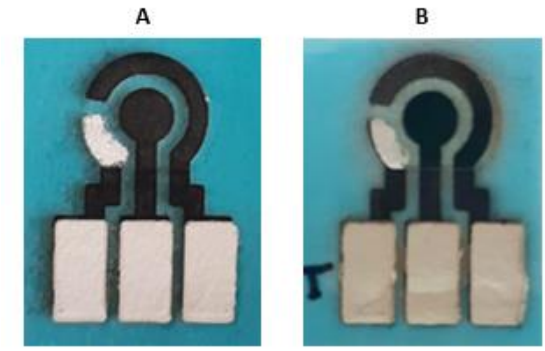

Figure 38 - **A)** pH sensor **B)** pH sensor after the PANI electropolymerization.

To complement the visual analysis of the WE that suggested an effective electropolymerization of PANI, SEM and EDS were performed to characterize morphologically and chemically the modified LIG WE area. On the SEM images captured it was very difficult to identify the morphological alterations on the LIG surface provoked by PANI electropolymerization, revealing that LIG structure was not compromised during the deposition process. The chemical formula of PANI is $(C_6H_5N)_X$ in such manner when the EDS technique was used to study the WE area of the pH sensor, the chosen chemical elements to be quantified were carbon and nitrogen.

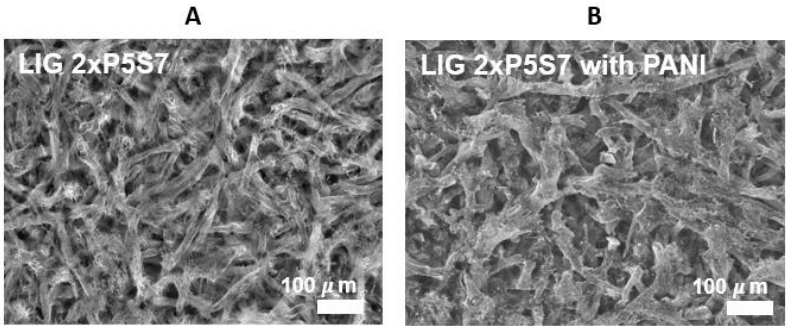

Figure 39 - SEM images of **A)** LIG on paper sample with 2 laser scans of 5% of the power and 7% of the laser speed **B)** PANI electropolimerized WE on a LIG on paper sample with 2 laser scans of 5% of the power and 7% of the laser speed.

The EDS image of the WE area showed that carbon was widely present in the analyzed area, while nitrogen was present in less quantity than carbon and homogeneously distributed. Additionally, through the EDS analysis of the relative atomic percentage of carbon and nitrogen on the PANI electropolymerized on a LIG WE, it was identified a very significant presence of nitrogen in the WE area in comparison with LIG whose nitrogen concentration is residual due to the break of bonds that occurred due to the laser irradiation. The significant expression of the nitrogen in the WE area indicates the immobilization of nitrogen atoms on surface of LIG on paper which corroborates the hypothesis of effective PANI electropolymerization of the WE.

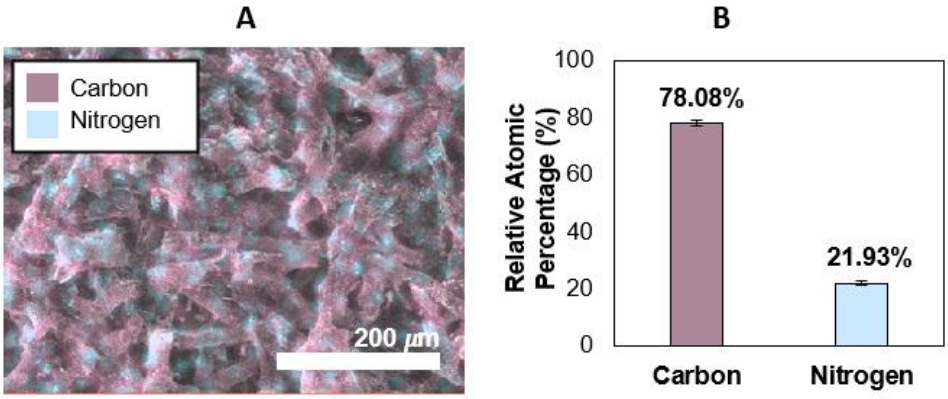

Figure 40 - **A)** EDS image of the spatial distribuition of carbon and nitrogen on a PANI eletropolimerized LIG sample. **B)** Relative Atomic Percentage of carbon and nitrogen on a PANI eletropolimerized LIG sample.

5.3.1. LIG on Paper pH Measuring Properties

The pH sensor developed in this dissertation work is based on the chemical reactions that occur in the electrochemical cell working area and analyte solution, which generates a potential difference between the RE and WE variations that can be measured [68][82][131].

The pH sensor was tested using the OCP technique by dropcasting different BR buffer solutions on the sensor working area. Before each test, the sensor was calibrated by recording the OCP of the first solution until the measured potential stabilizes.

To obtain the OCP sensor response in BR buffer solutions between 2 pH and 9 pH on **Figure 41A)**, after the sensor stabilization, 50 seconds of the first solution is recorded and then removed with a paper tissue. Then, the next solution is dropcasted and the OCP measurement occurs through the following 50 seconds. This procedure is then repeated for each solution and the respective pH level is registered. The graph on **Figure 41A)** allow the analysis of the response of the sensor when switching between buffer solutions with different pH. The sensor drastically alters its electromotive force in the first instant, but then rapidly stabilizes. The pH sensor demonstrated a linear response, whose sensitivity is $51.5\,mV/pH$, with $2.3\,mV/pH$ of standard deviation with $R^2 = 0.988$. To study the reproducibility of the sensor, 4 samples were measured whose resulting standard calibration curves appear in **Figure 41B)**. The average sensitivity of 4 pH sensor samples is $53.0\,mV/pH$ with $2.3\,mV/pH$ of standard deviation that corresponds to 4% of RSD. The average standard electrode potential of $319.1\,mV$ with $13.8\,mV$ of standard deviation that corresponds to 4% of RSD. These results show that the developed sensors have good pH sensor reproducibility, which is crucial for validating the sensor fabrication process. Nonetheless, the reproducibility of sensor performance can be further improved by standardizing and regulating the sensor fabrication steps and conducting studies about the electrochemical performance of the sensors and the performance of sensor calibration.

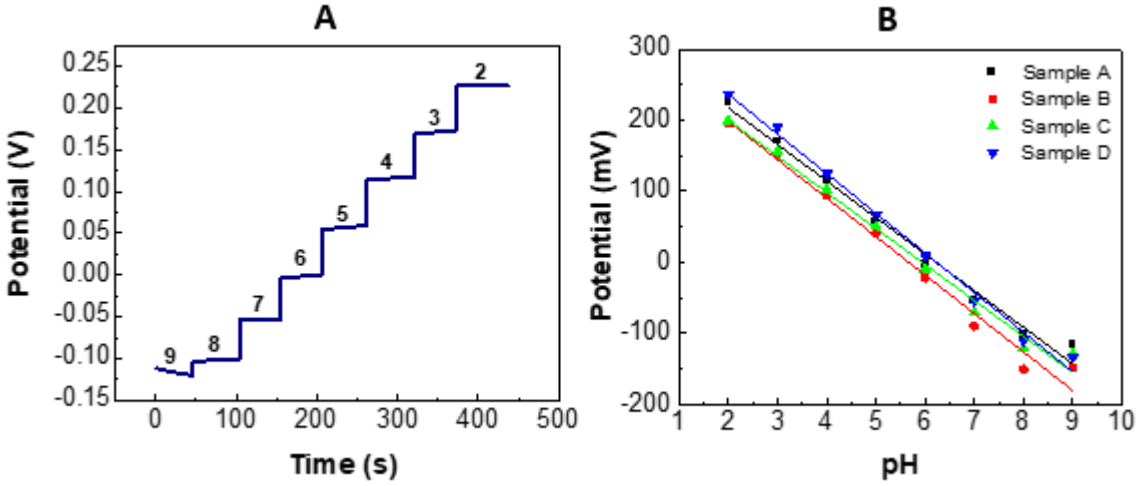

Figure 41 - **A)** pH sensor OCP response to BR buffer solutions between 2 pH and 9 pH. **B)** Reproducibility test of pH sensor measured in buffered solutions between 2 pH and 9 pH.

Sensor stability is an important parameter to be analyzed in the sensor performance. Especially in this case, once the pH sensor will be incorporated within the wound dressings and its measurement must not be impaired by the exposure time. This parameter was tested by measuring the potential for each previously prepared dropcasted BR solution between 2

pH and 9 pH in 180 seconds, an interval 4.5 times longer than the previously used. The sensor performance is highly stable, without suffering significant alterations, as it can be seen in **Figure 42**. The main standard deviation obtained for this sensor was $0.5\,mV/pH$, that corresponds to 0.7% of RSD. The sensor was demonstrated to be highly stable. However further studies about the sensor stability with longer exposure times must be realized, once the wound dressings change frequency is in most cases daily, but it depends on the DFU healing state.

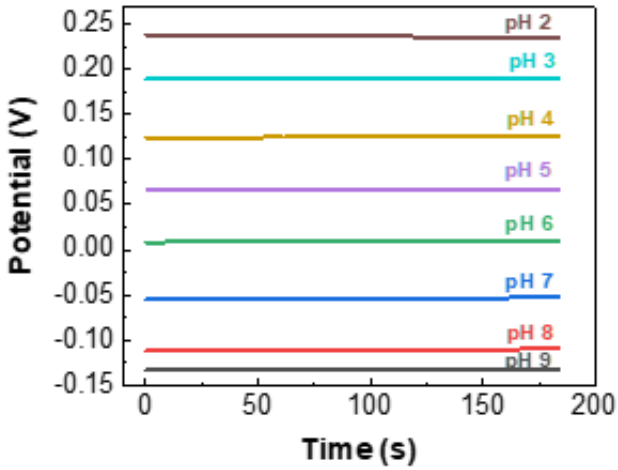

Figure 42 - Long term stability test of the pH sensor.

The sensor repeatability performance was tested through 3 consecutive OCP measurements of a sequence of four BR solutions whose pH are from 5 to 8, **Figure 43A)**. The sensitivity of the sensor used for this test was $-49.2\,mV/pH$ with $5.8\,mV/pH$ of standard deviation and intercept of $285.0\,mV$ with $38.4\,mV$ of standard deviation. To study the influence of the usage of the sensor with the potential measured, namely the hysteresis effect, it was measured the potential evoked within a sequence of descending and ascending pH of three BR buffer solutions, with 5 pH, 7 pH, and 9 pH, in the working area, represented on **Figure 43B)**. The sensor had a very linear behavior, and the sensor sensitivity was very close to the Nernstian limit. Respectively the R^2 of the sensor corresponds to 0.993, and its sensitivity is given by $-55.8\,mV/pH$ with $4.8\,mV/pH$ of standard deviation, and lastly an intercept of $330.3\,mV$ with $34.8\,mV$.of standard deviation. The sensor demonstrated repeatability needs to be improved because the average RSD of potential measurements of the solutions with the same pH was 8%, which means a slight discrepancy. However, it can be improved by calibrating the sensor for longer periods of time. Moreover, the sensor demonstrated to not be significantly affected by the hysteresis effect, once the average RSD of 3 measurements of each same pH solution was 3%, demonstrating a very small variation of the potential measured with solutions with the same pH, with ascending and descending sequences that subsequently shows good reversibility.

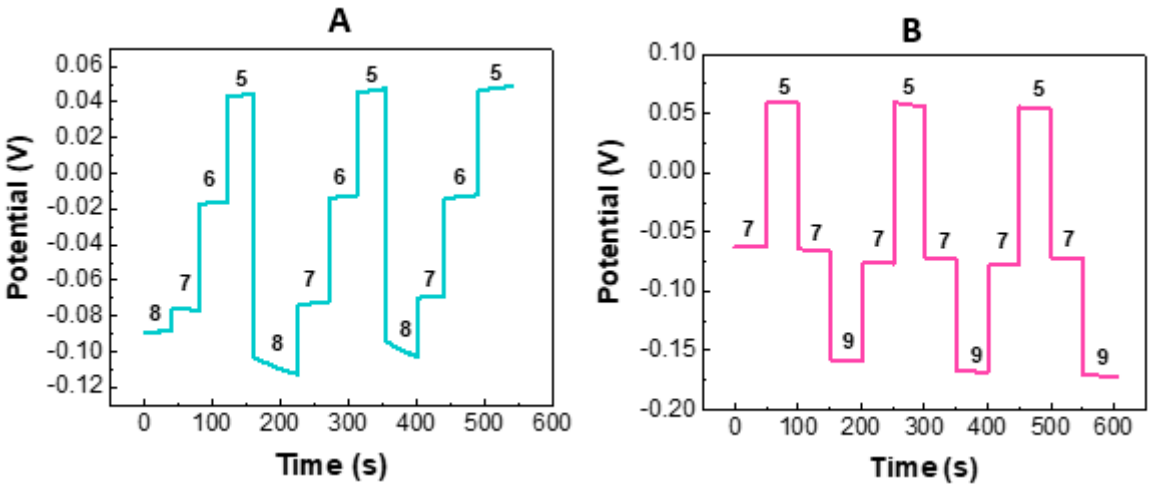

Figure 43 - **A)** Repeatibility test of the potentiometric pH sensor within the pH range of 5 pH to 8 pH. **B)** Hysteris test of the pH sensor from 5 pH to 9 pH.

Table 3 has aim to facilitate the comparison of the pH sensing performance of the sensors developed in this dissertation with reported potentiometric sensors using PANI as pH-sensitive material using diverse types of substrates and WE modification techniques. The sensitivity and linearity of the pH sensors produced in this work are comparable with the sensitivity and linearity of the other approaches. Comparing the sensitivity of the sensor developed with sensors that used LIG modified the WE with electropolymerization of PANI, it can be concluded that the sensor developed has higher sensitivity than the PI-LIG pH sensor developed by Liao et al. [98], but has significantly lower sensitivity than LIG written on PI and transferred to polydimethylsiloxane (PDMS) pH sensor developed by Xuan group [97], that has a super-*Nernstian* behavior by exceeding the theoretical maximum sensitivity at room temperature given by $-59\,mV/pH$. This behavior was also observed by the PANI sensor on reduced graphene oxide [128]. Additionally, the sensor developed has a similar but higher sensitivity than the sensor whose carbon WE was modified by coating PANI with palette paper, an analogous substrate with Whatman paper, produced by Rahimi team [132]. Summing up, the pH sensor performance is similar to pH sensors developed by the scientific community using PANI as sensitive material in recent years. However, the sensor developed in this dissertation has the advantages of using LIG, a simpler fabrication technique to produce the electrodes, and uses paper, a sustainable, abundant, and low-cost material, as the substrate.

Table 3 - Comparison of the absolute pH sensitivity between different sensor approaches.

Sensor	Substrate	PANI Deposition on WE	Range (pH)	Sensitivity (mV/pH)	R^2	Reference
LIG-PANI	PDMS	Electropolymerization	$[4,7]$	66	0.999	[97]
Carbon-PANI	PET	Screen Printing	$[3.9,10.1]$	62.4	0.9984	[73]
rGO-PANI	ITO-PET	Electropolymerization	$[2,8]$	62.3	-	[128]
Carbon-PANI	Bandage	Electropolymerization	$[2.69,8.51]$	59.2	-	[99]
Carbon-PANI	Textiles	Electropolymerization	$[3,10]$	55.4	0.9954	[133]
LIG-PANI	Whatman Paper	Electropolymerization	$[2,9]$	53.0	0.988	This work
Platinum-PANI	Glass sheath	Electropolymerization	$[2,11]$	52.0	0.9573	[134]
LIG-PANI	PI	Electropolymerization	$[4,7]$	51.5	-	[98]
Carbon-PANI	Palette paper	Coated	$[4,10]$	50.0	0.9734	[132]
Carbon-PANI	Textiles	Screen-printing	$[3,10]$	28.2	0.9971	[133]

6. Conclusions and Future Work

The work developed in this dissertation demonstrated that LIG fabrication technique could be applied to develop flexible, lightweight, wearable, biocompatible, sustainable, and low-cost temperature, and pH sensors on the physiologically meaningful interval of temperature and pH to be incorporated on a point of care platform that monitors the DFU healing state and predicts wound infections.

The work developed in this dissertation started with the optimization of the LIG on paper technique through its characterization, then LIG on paper temperature sensors were developed and their electrical performance was studied. Moreover, pH sensors were developed, and their electrochemical behavior was analyzed. The conclusions achieved in each section of the work will be presented.

Firstly, before the production of the sensors, the LIG production technique was optimized through the chemical, structural and electrical characterization of LIG produced with different laser parameters combinations. The optical analysis of the LIG produced with different combinations of laser power and scanning speed with one or two laser irradiations resulted in the formation of three laser irradiation effects on the substrate. When the laser power was lower than the scanning speed, the energy of the laser irradiation didn't induce the cellulose to graphene conversion. Furthermore, ablation of the substrate occurred when the laser power was higher than the energy of the laser irradiation absorbed by the laser speed was so high it provoked the breakdown of all connections. Lastly, graphitization of the substrate did occur when the laser power and laser speed had the same or slightly higher percentage. The latter laser conditions were subsequently analyzed through a 4-point probe technique to characterize LIG conductivity by measuring the sheet resistance. The conductivity of LIG is intrinsically related to the number of defects it presents, therefore the most conductive samples were then additionally characterized chemically and structurally. Through the identification and analysis of the characteristic LIG peaks on the Raman spectra, we could verify the effective LIG synthetization, the number of graphene layers formed, and the amount of structural defect under different conditions. The resulting SEM images demonstrated the paper-LIG rugous, and porous surface resulted from chemical bond breakdown and liberation of the elements on the gaseous form through cellulose fibers. Then, EDS quan-

tified the relative percentage of elements on paper-LIG samples and presented its spatial distribution, allowing us to verify the presence of LIG on the substrate. The LIG samples produced with two lasing scans demonstrated lower sheet resistance, indicating more graphitization of the substrate. The laser condition that leads to the formation of the most conductive LIG was 2 laser scans with 6% of the laser power and 8% of the laser speed and its corresponding sheet measurement was $16.2 \pm 2.0\ \Omega/sq$.

After the LIG on paper optimization, LIG technique was used to produce temperature sensors. The sensors' performance was defined by the measurement of the current that crosses the sensitive area, while a known tension value is applied throughout the time the sensor is at a specific temperature. The LIG laser parameter combination which showed lower sheet resistivity was first used on the temperature sensors. However, this condition provokes the formation of an extremely porous material, highly prone to suffer from ruptures conditioning the sensor measurement. Consequently, the LIG production parameters were altered to 2 laser scans of 5% of the laser power and 7% of the laser scanning speed. Diminishing the interference of the contact between the measurement unit and the sensor electrode area was a challenge for the electrical characterization. The first material used to connect the sensor was copper adhesive tape to the measurement unit. The adhesion of the copper tape to the electrode area was weak and unstable during the measurement, highly interfering with the data obtained. Also, the mechanical tension applied by the crocodile tips frequently deformed the material, causing its rupture or detachment from the electrode area, including the silver ink and graphene, from the paper substrate. Alternately, the copper adhesive tape was replaced by the silver wires, whose adhesion to the electrode area was more stable, due to its higher strength, and the measurement of the electrical features wasn't affected as much by the deformation of the silver wires induced by the mechanical tension applied. However, the separation of the intermediate contact from the electrode area still occurred. Relatively to the sensor design, it was possible to conclude that the sensors developed with the largest area, although were more sensitive to the temperature variation, their sensitivity was 1.49% $°C^{-1}$. Nonetheless, the production of these sensors was time-consuming, the sensors produced were fragile and this design wasn't adequate to be incorporated into a bandage to test *in vivo* rodent model. Therefore, two designs with smaller irradiated areas were studied. Of the two smaller sensors, the sensor that demonstrated higher sensitivity, and less variability was the sensor with the bigger sensitive area, whose sensitivity was 0.71%$°C^{-1}$. Due to the experimental setup limitations related to the contact between the sensor and measuring unit, sensors that could be fully electrically characterized within the temperature interval without suffering interference were very few, and its measurement occurred mainly on different days, with different environment humidity. The sensor with the smallest irradiated area was electrically characterized between the entire interval without disturbance in 4 samples. This sensor demonstrated to have different electrical behavior, with different resistance at room temperature, whose RSD is 15%, and different variations of electrical resistance with temperature with 35% of RSD. However, we could separate these four samples into two different groups,

the samples that were produced on the same day and measured on different days had similar electrical behavior with the variation of temperature but had different resistance in the temperature room. And the samples that were measured on the same day but had been produced on different days had similar resistance at room temperature but a different variation of resistance. This leads to the conclusion that the sensors must be highly sensitive to the environmental humidity at the time the measurement occurred. A variable that was first overlooked once the sensors were encapsulated with laminated pouches. To observe the quality of the sensor encapsulation, the sensor's electrical performance was analyzed while varying the relative humidity of the chamber where the sensor was placed. We concluded that the sensor's electrical behavior altered significantly. And other encapsulation options should be considered.

Summing the temperature sensors up, LIG on paper is electrically sensitive to the variation of temperature, demonstrating a linear decrease of electrical resistance with the increasing temperature. However, the sensitivity of the sensors with a design adaptable to tested *in vivo* rodent models is low in the physiologically significant interval. The analysis of the sensor reproducibility is corrupted due to the measurement setup limitations that derailed the performance of the sensor. The reliability of the sensor was also impaired due to the sensor sensitivity to the relative humidity that influenced the sensor behavior.

In follow up the LIG on paper technique was utilized to develop an electrochemical cell with 2 laser scan of 5% of the laser power and 7% of the laser scanning speed and the WE were PANI electropolymerized to produce a potentiometric pH sensor. The electrochemical performance of the pH was tested by performing OCP while the working area of the sensor had a drop cast solution of BR buffer solutions between the 2pH and 9pH. The reproducibility of the sensor was tested on 4 samples whose average sensitivity was $53.0\ mV/pH$ with $2.3\ mV/pH$ of standard deviation which corresponds to 4% of RSD and standard electrode potential of $319.1\ mV$ with $13.81\ mV$ of standard deviation that corresponds to 4% of RSD, which demonstrates great reproducibility. Additionally, the pH measurement of the sensor demonstrates to be very stable. It was tested by recording the potential of a sensor during a longer time intervals (180 seconds), the average standard deviation of the solution was 0.5 mV. The sensor repeatability performance was tested with 4 BR solutions from 8pH to 5pH whose sequence was tested 3 consecutive times, the RSD of the sensor was 8%, its sensitivity $-49.2\ mV/pH$ with $5.8\ mV/pH$ of standard deviation and intercept of $285.0\ mV$ with $5.8\ mV$ of standard deviation. And lastly, the study of hysteresis effect on the pH measurement was performed with 3 BR solutions whose pH are between 5 and 9 pH with a 2pH difference between them. The standard deviation of the sensor was 3%, which demonstrated that the sensor was not affected by the hysteresis effect. The sample used for this characterization had the closest sensitivity to the *Nernstian* limit, $-55.8\ mV/pH$ with $4.8\ mV/pH$ of standard deviation and intercept of $330.3\ mV$ with $34.8\ mV$ of standard deviation.

To sum up, the results of the pH sensor characterization are highly satisfying, they have adequate sensitivity very close to the *Nernstian* limit, are reproducible, have a good repeata-

ble performance, and demonstrated to not be heavily affected by the hysteresis effect. These results demonstrate that LIG on paper techniques are a great option to develop pH sensors.

Despite the satisfactory performance obtained in this study, the sensor's fabrication and performance analysis could be improved. In particular, the temperature sensors need to be further studied and optimized. The experimental setup of measurement must be updated and standardized to minimize human error, the electrical connection must be adapted to not interfere with the characterization, and the data acquisition must be automated so it isn't prone to human error. This update will allow and ease the characterization of the sensor durability, repeatability, hysteresis, response time, and recovery time. Another type of sensor encapsulation must be explored for effective isolation. However, if the sensor's effective encapsulation is not possible, the electrical characterization of the sensor with the variation of temperature and relative humidity must be studied simultaneously. Additionally, the pH sensor's fabrication steps and performance techniques could be optimized and studied. Although the pH sensor sensitivity was adequate, another LIG fabrication condition could have improved electrochemical performance. Also, the electropolymerization of the WE could be optimized to lead to better sensing results. To supplement the validation of the pH sensor's behavior, the sensors should be studied with natural or artificial wound exudate sample trails.

A future prospective of the sensors is its incorporation into an environmentally friendly wearable point of care device that could be included on the wound dressings to monitor the DFU healing state. If other techniques of sensor encapsulation don't work on the thermoresistive sensor, their incorporation on the point of care platform must be accompanied by the integration of a humidity sensor to aid the decipherment of the DFU temperature by resistance change of the sensor. This platform must incorporate a flexible wireless circuit board that could be projected to perform measurement and data acquisition, which includes a portable potentiostat and current measurement unit. Additionally, the platform could include a smartphone application that receives the measured data, shows the result to the user, and could send a report to the physician remotely. One of the aims of the Santander project, where the work of this dissertation is included, consisted of testing the sensors developed *in vivo* rodent models, that due to the anatomical and physiological similarities between humans and animals, it is possible to study the DFU wound healing process. Therefore, during the semester I attended CONGENTO Theory Course in Laboratory Animal Science and IGC's Practical Course on Laboratory Animal Science in Mouse to obtain the knowledge to realize the procedures that need to be performed on the animal models, after understanding its physiological and ethical implications. In the Appendix I present the Certificate of the CONGENTO Theory Course in Laboratory Animal Science and the Certificate of the IGC's Practical Course on Laboratory Animal Science in Mouse. However, due to time constraints and a delay in the Ethics Committee approval, this part of the project was not achieved.

BIBLIOGRAPHY

[1] J. E. H. Arthur C. Guyton, "Insulin, Glucagon, and Diabetes Mellitus," in *Textbook of Medical Physiology*, 11th ed., A. Guyton and J. Hall, Eds. Philadelphia, Pennsylvania: Elsevier, 2006, pp. 961–976.

[2] J. L. Jameson, "Diabetes Mellitus," in *Harrison's Endocrinology*, J. L. Jameson, Ed. Philadelphia, Pennsylvania: McGraw-Hill Education, 2013, pp. 261–307.

[3] D. Magliano, E. Koyko, B. Balkau, and N. Barengo, "Diabetes prevalence," in *IDF Diabetes Atlas*, 10th ed., E. Boyko, D. Magliano, S. Karunga, and L. Piemonte, Eds. 2021, pp. 34–38.

[4] W. D. Aumiller and H. A. Dollahite, "Pathogenesis and Management of Diabetic Foot Ulcers," *American Academy of Physician Assistants*, vol. 28, no. 5, pp. 28–34, 2015.

[5] A. Perez-Favila *et al.*, "Current therapeutic strategies in diabetic foot ulcers," *Medicina (Lithuania)*, vol. 55, no. 11, pp. 1–21, 2019.

[6] E. Gianino, C. Miller, and J. Gilmore, "Smart wound dressings for diabetic chronic wounds," *Bioengineering*, vol. 5, no. 3, 2018.

[7] M. Syndrome, "Incidence of Diabetic Foot Ulcer and Its Predictors Among Diabetes Mellitus Patients at Felege Hiwot Referral Hospital , Bahir Dar , Northwest Ethiopia : A Retrospective Follow-Up Study," pp. 3703–3711, 2020.

[8] C. Saliba Thorne, A. Gatt, C. DeRaffaele, A. Bazena, and C. Formosa, "Digital foot health technology and diabetic foot monitoring: A systematic review," *Diabetes Research and Clinical Practice*, vol. 175, p. 108783, 2021.

[9] J. Golledge, M. Fernando, P. Lazzarini, and B. Najafi, "The Potential Role of Sensors, Wearabes and Telehelth in the Remote Management of Diabetes-Related Foot Disease," *Sensors*, vol. 20, no. 16, 2020.

[10] A. Raghav, Z. A. Khan, R. K. Labala, J. Ahmad, S. Noor, and B. K. Mishra, "Financial burden of diabetic foot ulcers to world: a progressive topic to discuss always," *Therapeutic Advances in Vaccines*, vol. 9, no. 6, pp. 259–261, 2018.

[11] L. A. Lavery, O. K. Oz, K. Bhavan, and D. K. Wukich, "Diabetic Foot Syndrome in the Twenty-First Century," *Clinics in Podiatric Medicine and Surgery*, vol. 36, no. 3, pp. 355–359, 2019.

[12] M. Yavuz *et al.*, "Temperature as a Causative Factor in Diabetic Foot Ulceration: A Call to Revisit Ulcer Pathomechanics," *Journal of the American Podiatric Medical Association*, vol. 109, no. 5, pp. 345–350, 2018.

[13] S. Ostadabbas, A. Saeed, M. Nourani, and M. Pompeo, "Sensor architectural tradeoff for diabetic foot ulcer monitoring," *Proceedings of the Annual International Conference of the IEEE Engineering in Medicine and Biology Society, EMBS*, pp. 6687–6690, 2012.

[14] L. A. Schneider, A. Korber, S. Grabbe, and J. Dissemond, "Influence of pH on wound-healing: A new perspective for wound-therapy?," *Archives of Dermatological Research*, vol. 298, no. 9, pp. 413–420, 2007.

[15] M. Tessarolo *et al.*, "Wireless Textile Moisture Sensor for Wound Care," *Frontiers in Physics*, vol. 9, no. 722173, pp. 1–9, 2021.

[16] S. Roy *et al.*, "An Electroanalytical Paper-Based Wound Dressing Using ZIF-67/C3N4Nanocomposite towards the Monitoring of Staphylococcus Aureus in Diabetic Foot Ulcer," *IEEE Sensors Journal*, vol. 21, no. 2, pp. 1215–1221, 2021.
[17] C. Renero and J. Francisco, "The abrupt temperature changes in the plantar skin thermogram of the diabetic patient: looking in to prevent the insidious ulcers," *Diabetic Foot and Ankle*, vol. 9, no. 1. 2018.
[18] J. Selle J, A. Aminuddin, and K. Chellappan, "Benefit of Foot Thermogram Analysis in the Treatment of Diabetic Foot Ulcer: A Systematic Review," *Biomedical Research and Therapy*, vol. 9, no. 5, pp. 5029–5042, 2022.
[19] H. Maldonado, R. Bayareh, I. A. Torres, A. Vera, J. Gutiérrez, and L. Leija, "Automatic detection of risk zones in diabetic foot soles by processing thermographic images taken in an uncontrolled environment," *Infrared Physics and Technology*, vol. 105, no. January, p. 103187, 2020.
[20] K. J. Farid, C. Winkelman, A. Rizkala, and K. Jones, "Using temperature of pressure-related intact discolored areas of skin to detect deep tissue injury: An observational' retrospective' correlational study," *Ostomy Wound Management*, vol. 58, no. 8, pp. 20–31, 2012.
[21] S. D. Milne *et al.*, "A wearable wound moisture sensor as an indicator for wound dressing change: An observational study of wound moisture and status," *International Wound Journal*, vol. 13, no. 6. pp. 1309–1314, 2016.
[22] C. Scott, S. Cameron, J. Cundell, A. Mathur, and J. Davis, "ScienceDirect Electrochemistry Adapting resistive sensors for monitoring moisture in smart wound dressings," *Current Opinion in Electrochemistry*, vol. 23, pp. 31–35, 2020.
[23] L. A. Wallace, L. Gwynne, and T. Jenkins, "Challenges and opportunities of pH in chronic wounds," *Therapeutic Delivery*, vol. 10, no. 11, pp. 719–735, 2019.
[24] E. Jones, C. Cochrane, and S. Percival, "The Effect of pH on Extracellular Matrix and Biofilms," *Advances in Wound Care*, vol. 4, no. 7, pp. 431–439, 2015.
[25] C. Mcardle, K. M. Lagan, and D. A. Mcdowell, "The pH of Wound Fluid in Diabetic Foot Ulcers-the Way Forward in Detecting Clinical Infection?," *Current Diabetes Reviews*, vol. 10, pp. 177–181, 2014.
[26] "Disposable Paper-Based Biosensors: Optimizing the Electrochemical Properties of Laser-Induced Graphene," *Applied Materials and Interfaces*, vol. 14, no. 27, pp. 31109–31120, 2022.
[27] R. Ye, D. K. James, and J. M. Tour, "Laser-Induced Graphene: From Discovery to Translation," *Advanced Materials*, vol. 31, no. 1, pp. 1–15, 2019.
[28] A. Samouco, A. C. Marques, A. Pimentel, R. Martins, and E. Fortunato, "Laser-induced electrodes towards low-cost flexible UV ZnO sensors," *Flexible and Printed Electronics*, vol. 3, no. 4, 2018.
[29] T. Pinheiro *et al.*, "Laser-Induced Graphene on Paper toward Efficient Fabrication of Flexible, Planar Electrodes for Electrochemical Sensing," 2021.
[30] B. Kulyk *et al.*, "Laser-Induced Graphene from Paper for Mechanical Sensing," 2021.
[31] M. L. Salva, M. Rocca, C. M. Niemeyer, and E. Delamarche, "Methods for immobilizing receptors in microfluidic devices: A review," *Micro and Nano Engineering*, vol. 11, no. April, 2021.
[32] L. Wang *et al.*, "A Review of Wearable Sensor Systems to Monitor Plantar Loading in

the Assessment of Diabetic Foot Ulcers," *IEEE Transactions on Biomedical Engineering*, vol. 67, no. 7, pp. 1989–2004, 2020.
[33] H. Derakhshandeh, S. S. Kashaf, F. Aghabaglou, I. O. Ghanavati, and A. Tamayol, "Smart Bandages: The Future of Wound Care," *Trends in Biotechnology*, vol. 36, no. 12, pp. 1259–1274, 2018.
[34] M. Chakraborty and M. S. J. Hashmi, "Graphene as a Material – An Overview of Its Properties and Characteristics and Development Potential for Practical Applications," *Reference Module in Materials Science and Materials Engineering*, pp. 24–26, 2018.
[35] T. Premkumar and K. E. Geckeler, "Graphene-DNA hybrid materials: Assembly, applications, and prospects," *Progress in Polymer Science (Oxford)*, vol. 37, no. 4, pp. 515–529, 2012.
[36] H. Huang *et al.*, "Graphene-based sensors for human health monitoring," *Frontiers in Chemistry*, vol. 7, no. JUN, pp. 1–26, 2019.
[37] J. Liu *et al.*, "Laser-induced graphene (LIG)-driven medical sensors for health monitoring and diseases diagnosis," *Microchimica Acta*, vol. 189, no. 2, 2022.
[38] C. Zhu *et al.*, "Graphene oxide humidity sensor with laser-induced graphene porous electrodes," *Sensors and Actuators, B: Chemical*, vol. 325, no. May, p. 128790, 2020.
[39] A. Kaidarova and J. Kosel, "Physical Sensors Based on Laser-Induced Graphene: A Review," *IEEE Sensors Journal*, vol. 21, no. 11, pp. 12426–12443, 2021.
[40] H. Wang, Z. Zhao, P. Liu, and X. Guo, "Laser-Induced Graphene Based Flexible Electronic Devices," *Biosensors*, vol. 12, no. 2, 2022.
[41] Y. Chyan, R. Ye, Y. Li, S. P. Singh, C. J. Arnusch, and J. M. Tour, "Laser-Induced Graphene by Multiple Lasing: Toward Electronics on Cloth, Paper, and Food," *ACS Nano*, vol. 12, no. 3, pp. 2176–2183, 2018.
[42] A. Tuttolomondo, C. Maida, and A. Pinto, "Diabetic foot syndrome: Immune-inflammatory features as possible cardiovascular markers in diabetes," *World Journal of Orthopedics*, vol. 6, no. 1, pp. 62–76, 2015.
[43] S. Spiliopoulos, G. Festas, I. Paraskevopoulos, M. Mariappan, and E. Brountzos, "Overcoming ischemia in the diabetic foot: Minimally invasive treatment options," *World Journal of Diabetes*, vol. 12, no. 12, pp. 2011–2026, 2021.
[44] D. F. Bandyk, "The diabetic foot: Pathophysiology, evaluation, and treatment," *Seminars in Vascular Surgery*, vol. 31, no. 2–4, pp. 43–48, 2018.
[45] A. Berbudi, N. Rahmadika, A. I. Tjahjadi, and R. Ruslami, "Type 2 Diabetes and its Impact on the Immune System," *Current Diabetes Reviews*, vol. 16, no. 5, pp. 442–449, 2019.
[46] M. Edmonds, "Diabetic Foot Ulcers-Practical Treatment Recommendations," *Drugs*, vol. 66, no. 7, pp. 913–929, 2006.
[47] M. Monteiro-Soares *et al.*, "Guidelines on the classification of diabetic foot ulcers (IWGDF 2019)," *Diabetes/Metabolism Research and Reviews*, vol. 36, no. S1. 2020.
[48] J. Burgess, W. Wyant, and B. A. Abujamra, "Diabetic Wound-Healing Science," *MDPI Medicina*, vol. 57, no. 1072, pp. 1–24, 2021.
[49] S. F. Spampinato, G. I. Caruso, R. De Pasquale, M. A. Sortino, and S. Merlo, "The treatment of impaired wound healing in diabetes: Looking among old drugs," *Pharmaceuticals*, vol. 13, no. 4. 2020.
[50] S. Patel, S. Srivastava, M. R. Singh, and D. Singh, "Mechanistic insight into diabetic

wounds: Pathogenesis, molecular targets and treatment strategies to pace wound healing," *Biomedicine and Pharmacotherapy*, vol. 112. 2019.
[51] X. Ding *et al.*, "Challenges and innovations in treating chronic and acute wound infections: from basic science to clinical practice," *Burns and Trauma*, vol. 10. 2022.
[52] T. Swanson, D. Angel, G. Sussman, and R. Cooper, "Wound Infection in Clinical Practice," *International Wound Journal*, 2016.
[53] S. Darvishi, S. Tavakoli, M. Kharaziha, H. H. Girault, C. F. Kaminski, and I. Mela, "Advances in the Sensing and Treatment of Wound Biofilms," *Angewandte Chemie - International Edition*, vol. 61, no. 13, 2022.
[54] G. Power, Z. Moore, and T. O'Connor, "Measurement of pH, exudate composition and temperature in wound healing: a systematic review," *Journal of Wound Care*, vol. 26, no. 7, pp. 381–397, 2017.
[55] P. Salvo, N. Calisi, and et al., "Temperature-and pH-sensitive wearable materials for monitoring foot ulcers," *International Journal of Nanomedicine*, vol. 12, no. January, pp. 949–954, 2017.
[56] A. J. Bullock, M. Garcia, J. Shepherd, I. Rehman, and M. Sheila, "Bacteria induced pH changes in tissue-engineered human skin detected non-invasively using Raman confocal spectroscopy," *Applied Spectroscopy Reviews*, vol. 55, no. 2. pp. 158–171, 2020.
[57] K. Roback, "An overview of temperature monitoring devices for early detection of diabetic foot disorders," *Expert Review of Medical Devices*, vol. 7, no. 5, pp. 711–718, 2010.
[58] Q. Pang *et al.*, "Smart Flexible Electronics-Integrated Wound Dressing for Real-Time Monitoring and On-Demand Treatment of Infected Wounds," *Advanced Science*, vol. 7, no. 6, 2020.
[59] N. Tang *et al.*, "Wearable sensors and systems for wound healing-related ph and temperature detection," *Micromachines*, vol. 12, no. 4, pp. 1–15, 2021.
[60] A. M. Wijlens, S. Holloway, S. A. Bus, and J. J. van Netten, "An explorative study on the validity of various definitions of a 2·2°C temperature threshold as warning signal for impending diabetic foot ulceration," *International Wound Journal*, vol. 14, no. 6, pp. 1346–1351, 2017.
[61] B. M. Schmidt, S. Allison, and J. S. Wrobel, "Describing Normative Foot Temperatures in Patients With Diabetes-Related Peripheral Neuropathy," *Journal of Diabetes Science and Technology*, vol. 14, no. 1. pp. 22–27, 2020.
[62] S. Bagavathiappan *et al.*, "Correlation between plantar foot temperature and diabetic neuropathy: A case study by using an infrared thermal imaging technique," *Journal of Diabetes Science and Technology*, vol. 4, no. 6. pp. 1386–1392, 2010.
[63] N. Bhalla, P. Jolly, N. Formisano, and P. Estrela, "Introduction to biosensors," *Essays in Biochemistry*, vol. 60, no. 1, pp. 1–8, 2016.
[64] V. Naresh and N. Lee, "A review on biosensors and recent development of nanostructured materials-enabled biosensors," *Sensors (Switzerland)*, vol. 21, no. 4, pp. 1–35, 2021.
[65] C. Gouvea, "Biosensors for health applications," *Biosensors for Health, Environment and Biosecurity*, 2011.
[66] J. Wilson, *Sensor Technology Handbook*, 1st ed. Newnes (Elsevier Inc.), 2005.

[67] X. Gong, L. Zhang, Y. Huang, and S. Wang, "Directly writing flexible temperature sensor with graphene nanoribbons for disposable healthcare devices," *The Royal Society of Chemistry*, vol. 10, no. 37, pp. 22222–22229, 2020.
[68] J. Fraden, *Handbook of Modern Sensors*, 4th editio. Springer New York, 2010.
[69] B. Xie and B. Danielsson, "Thermal Biosensor and Microbiosensor Techniques," *Handbook of Biosensors and Biochips*, 2008.
[70] T. Dinh, H.-P. Phan, A. Qamar, and P. Woodfield, "Thermoresistive Effect for Advanced Thermal Sensors : Fundamentals , Design Considerations , and Applications," *Journal of Microelectromechanical Systems*, vol. 26, no. 5, pp. 966–986, 2017.
[71] C. Karunakaran, K. Bhargava, and R. Benjamin, *Biosensors and Bioelectronics*, 1st editio. Elsvier, 2015.
[72] D. A. C. Brownson and C. E. Banks, *Handbook of Graphene Electrochemistry*, 1st editio. Manchester, UK: Springer London, 2014.
[73] H. J. Park, J. H. Yoon, K. G. Lee, and B. G. Choi, "Potentiometric performance of flexible pH sensor based on polyaniline nanofiber arrays," *Nano Convergence*, vol. 6, no. 1, 2019.
[74] I. Shitanda, H. Kiryu, and M. Itagaki, "Improvement in the long-term stability of screen-printed planar type solid-state Ag/AgCl reference electrode by introducing poly(dimethylsiloxane) liquid junction," *Electrochimica Acta*, vol. 58, no. 1, pp. 528–531, 2011.
[75] E. Zdrachek and E. Bakker, "Potentiometric Sensing," *Analytical Chemistry*, no. 91, pp. 2–26, 2019.
[76] A. C. Marques *et al.*, *Non-enzymatic lab-on-paper devices for biosensing applications*, 1st ed., vol. 89. Elsevier B.V., 2020.
[77] S. Amemiya *et al.*, *Handbook of Electrochemistry*, 1st editio. New Mexico, USA: Elsevier B.V., 2007.
[78] E. Gorbova, F. Tzorbatzoglou, C. Molochas, D. Chloros, A. Demin, and P. Tsiakaras, "Fundamentals and principles of solid-state electrochemical sensors for high temperature gas detection," *Catalysts*, vol. 12, no. 1, 2022.
[79] K. McLaughlin, N. P. Nezlin, and S. B. Weisberg, "An evaluation of potentiometric pH sensors in coastal monitoring applications," *Limnology and Oceanography: Methods*, vol. 15, no. 8, pp. 679–689, 2017.
[80] Y. Tang *et al.*, "Recent Advances in Wearable Potentiometric pH Sensors," *Membranes*, vol. 12, no. 5, pp. 1–20, 2022.
[81] L. Manjakkal, S. Dervin, and R. Dahiya, "Flexible potentiometric pH sensors for wearable systems," *RSC Advances*, vol. 10, no. 15. pp. 8594–8617, 2020.
[82] G. D. M. Madeira, H. J. Hugo, M. C. Faleiros, and M. Mulato, "Model improvement for super-Nernstian pH sensors: the effect of surface hydration," *Journal of Materials Science*, vol. 56, no. 3. pp. 2738–2747, 2021.
[83] S. Ravichandran, C. Thiagarajan, and P. S. Kumar, "pH Sensitivity Estimation in Potentiometric Metal Oxide pH Sensors Using the Principle of Invariance," *International Journal of Chemical Engineering*, vol. 2021, no. 5551259, pp. 1–18, 2021.
[84] Y. Yang and W. Gao, "Wearable and flexible electronics for continuous molecular monitoring," *Chemical Society Reviews*, vol. 48, no. 6. pp. 1465–1491, 2019.
[85] N. P. Shetti, A. Mishra, S. Basu, R. J. Mascarenhas, R. R. Kakarla, and T. M. Aminabhavi,

"Skin-Patchable Electrodes for Biosensor Applications: A Review," *ACS Biomaterials Science and Engineering*, vol. 6, no. 4, pp. 1823–1835, 2020.

[86] W. Gao, H. Ota, D. Kiriya, K. Takei, and A. Javey, "Flexible Electronics toward Wearable Sensing," *Accounts of Chemical Research*, vol. 52, no. 3. pp. 523–533, 2019.

[87] S. O'Callaghan, P. Galvin, C. O'Mahony, Z. Moore, and R. Derwin, "'Smart' wound dressings for advanced wound care: A review," *Journal of Wound Care*, vol. 29, no. 7, pp. 394–406, 2020.

[88] C. McArdle, K. Lagan, S. Spence, and D. McDowell, "Diabetic foot ulcer wound fluid: the effects of pH on DFU bacteria and infection," *Journal of Foot and Ankle Research*, vol. 8, no. S1, p. A8, 2015.

[89] M.-T. Tran, A. Kumar, A. Sachan, M. Castro, W. Allegre, and J.-F. Feller, "Emerging Strategies Based on Sensors for Chronic Wound Monitoring and Management," *Chemosensors*, vol. 10, no. 8, p. 311, 2022.

[90] J. Štulík, O. Musil, F. Josefík, and P. Kadlec, "Graphene-Based Temperature Sensors–Comparison of the Temperature and Humidity Dependences," *Nanomaterials*, vol. 12, no. 9, 2022.

[91] H. Kun, L. Bin, M. Orban, Q. Donghai, and Y. Hongbo, "Accurate Flexible Temperature Sensor Based on Laser-Induced Graphene Material," *Hindawi*, vol. 2021, no. 9938010, 2021.

[92] R. Han *et al.*, "Facile fabrication of rGO / LIG-based temperature sensor with high sensitivity," *Materials Letters*, vol. 304, no. July, p. 130637, 2021.

[93] B. Kulyk *et al.*, "Laser-Induced Graphene from Paper by Ultraviolet Irradiation: Humidity and Temperature Sensors," *Advanced Materials Technologies*, vol. 2101311, pp. 1–11, 2022.

[94] S. Gandla *et al.*, "Highly Linear and Stable Flexible Temperature Sensors Based on Laser-Induced Carbonization of Polyimide Substrates for Personal Mobile Monitoring," *Advanced Materials Technologies*, vol. 5, no. 7, pp. 1–9, 2020.

[95] Y. Zhang *et al.*, "Flexible integrated sensing platform for monitoring wound temperature and predicting infection," *Microbial Biotechnology*, vol. 14, no. 4, pp. 1566–1579, 2021.

[96] S. Gandla *et al.*, "Highly Linear and Stable Flexible Temperature Sensors Based on Laser-Induced Carbonization of Polyimide Substrates for Personal Mobile Monitoring," vol. 2000014, no. 7, pp. 1–9, 2020.

[97] X. Xuan, J. Y. Kim, X. Hui, P. S. Das, H. S. Yoon, and J. Y. Park, "A highly stretchable and conductive 3D porous graphene metal nanocomposite based electrochemical-physiological hybrid biosensor," *Biosensors and Bioelectronics*, vol. 120, no. August, pp. 160–167, 2018.

[98] J. Liao *et al.*, "Laser-Induced Graphene-Based Wearable Epidermal Ion-Selective Sensors for Noninvasive Multiplexed Sweat Analysis," 2022.

[99] T. Guinovart, G. Valdés-Ramírez, J. R. Windmiller, F. J. Andrade, and J. Wang, "Bandage-Based Wearable Potentiometric Sensor for Monitoring Wound pH," *Electroanalysis*, vol. 26, no. 6, pp. 1345–1353, 2014.

[100] A. Pal, D. Goswami, H. E. Cuellar, B. Castro, S. Kuang, and R. V. Martinez, "Early detection and monitoring of chronic wounds using low-cost, omniphobic paper-based smart bandages," *Biosensors and Bioelectronics*, vol. 117, no. June, pp. 696–705, 2018.

[101] S. Kumar, K. Bhatt, P. Kumar, S. Sharma, A. Kumar, and C. C. Tripathi, "Laser patterned, high-power graphene paper resistor with dual temperature coefficient of resistance," *RSC Advances*, vol. 9, no. 15, pp. 8262–8270, 2019.
[102] Departamento Ciência dos Materias, "João Coelho vencedor da 14ª Edição do Prémio de Investigação Colaborativa Santander/NOVA 2021," 2022. [Online]. Available: https://www.dcm.fct.unl.pt/noticias/2022/01/joao-coelho-vencedor-da-14-edicao-do-premio-de-investigacao-colaborativa-santandernova-2021. [Accessed: 22-Aug-2022].
[103] U. L. Systems, "VLS Desktop User Guide VLS2.30, VLS3.50," 2012.
[104] Universal Laser Systems, "Available Lenses," 2022. [Online]. Available: https://www.ulsinc.com/available-lenses.
[105] M. M. A. Khan, S. Saha, L. Romoli, and M. H. Kibria, "Optimization of laser engraving of acrylic plastics from the perspective of energy consumption, co2 emission and removal rate," *Journal of Manufacturing and Materials Processing*, vol. 5, no. 3, 2021.
[106] E. Gieva, G. Nikolov, and B. Nikolova, "Sheet Resistance Measurement of Inkjet Printed Layers," *Proceedings of the International Spring Seminar on Electronics Technology*, vol. 2019-May, pp. 1–6, 2019.
[107] M. Naftaly *et al.*, "Sheet resistance measurements of conductive thin films: A comparison of techniques," *Electronics (Switzerland)*, vol. 10, no. 8, 2021.
[108] Y. Seekaew, O. Arayawut, K. Timsorn, and C. Wongchoosuk, *Synthesis, characterization, and applications of graphene and derivatives*. Elsevier Inc., 2018.
[109] K. Akhtar, S. A. Khan, S. B. Khan, and A. M. Asiri, *Scanning Electron Microscopy : Principle and Applications in Nanomaterials Characterization*. 2018.
[110] K. D. Parry V, "Microscopy : An introduction," *III-Vs Review*, vol. 13, no. 4, pp. 40–44, 2000.
[111] M. Scimeca, S. Bischetti, and R. Bonfiglio, "Energy Dispersive X-ray (EDX) microanalysis: A powerful tool in biomedical research and diagnosis," *European Journal of Histochemistry*, vol. 62, no. 2841, pp. 89–99, 2018.
[112] M. Hu, Z. Yao, and X. Wang, "Characterization techniques for graphene-based materials in catalysis," *AIMS Materials Science*, vol. 4, no. 3, pp. 755–788, 2017.
[113] N. John and S. George, *Raman Spectroscopy*, vol. 2. Elsevier Inc., 2017.
[114] Metrohm, "Basic overview of the working principle of a potentiostat / galvanostat (PGSTAT) – Electrochemical cell setup," *Autolab Application Note EC08*, pp. 1–3, 2011.
[115] PalmsSens, "PalmSens4," *PalmSens*, 2022. [Online]. Available: https://www.palmsens.com/product/palmsens4/. [Accessed: 16-Aug-2022].
[116] Borax, "Borates for fire retardancy in cellulosic materials," vol. 12, pp. 1–12, 2021.
[117] E. Carrilho, A. W. Martinez, and G. M. Whitesides, "Understanding wax printing: A simple micropatterning process for paper-based microfluidics," *Analytical Chemistry*, vol. 81, no. 16, pp. 7091–7095, 2009.
[118] H. Park, M. Kim, B. G. Kim, and Y. H. Kim, "Electronic Functionality Encoded Laser-Induced Graphene for Paper Electronics," *ACS Applied Nano Materials*, vol. 3, no. 7, pp. 6899–6904, 2020.
[119] T. Pinheiro *et al.*, "Laser-Induced Graphene on Paper toward Efficient Fabrication of Flexible, Planar Electrodes for Electrochemical Sensing," *Advanced Materials Interfaces*, vol. 8, no. 22, pp. 1–12, 2021.
[120] Y. Chyan, J. Cohen, W. Wang, C. Zhang, and J. M. Tour, "Graphene Art," *ACS Applied*

Nano Materials, vol. 2, no. 5, pp. 3007–3011, 2019.
[121] E. R. Mamleyev *et al.*, "Laser-induced hierarchical carbon patterns on polyimide substrates for flexible urea sensors," *npj Flexible Electronics*, vol. 3, no. 1, 2019.
[122] G. Liu *et al.*, "A flexible temperature sensor based on reduced graphene oxide for robot skin used in internet of things," *Sensors (Switzerland)*, vol. 18, no. 5, 2018.
[123] C. Yan, J. Wang, and P. S. Lee, "Stretchable graphene thermistor with tunable thermal index," *ACS Nano*, vol. 9, no. 2, pp. 2130–2137, 2015.
[124] R. Resnick and J. Walker, "Fundamentos de Física - Eletromagnetismo," in *Fundamentos de Física - Eletromagnetismo*, 10th ed., R. S. Biasi, Ed. Rio de Janeiro: John Wiley & Sons, Inc., 2016, pp. 319–371.
[125] A. Yoshida, Y.-F. Wang, and S. Tachibana, "Printed, all-carbon-based flexible humidity sensor using a cellulose nanofiber/graphene nanoplatelet composite," *Carbon Trends*, vol. 7, 2022.
[126] V. P. Wanjari, A. S. Reddy, S. P. Duttagupta, and S. P. Singh, "Laser-induced graphene-based electrochemical biosensors for environmental applications: a perspective," *Environmental Science and Pollution Research*, no. 0123456789, 2022.
[127] I. S. Kucherenko *et al.*, "Laser-induced graphene electrodes for electrochemical ion sensing, pesticide monitoring, and water splitting," *Analytical and Bioanalytical Chemistry*, vol. 413, no. 25. pp. 6201–6212, 2021.
[128] F. Mazzara *et al.*, "Pani-based wearable electrochemical sensor for ph sweat monitoring," *Chemosensors*, vol. 9, no. 7, pp. 1–14, 2021.
[129] T. Lindfors and A. Ivaska, "pH sensitivity of polyaniline and its substituted derivatives," *Journal of Electroanalytical Chemistry*, vol. 531, no. 1, pp. 43–52, 2002.
[130] A. Korent, K. Žagar Soderžnik, S. Šturm, and K. Žužek Rožman, "A Correlative Study of Polyaniline Electropolymerization and its Electrochromic Behavior," *Journal of The Electrochemical Society*, vol. 167, no. 10, p. 106504, 2020.
[131] S. Ravichandran, C. Thiagarajan, and P. S. Kumar, "pH Sensitivity Estimation in Potentiometric Metal Oxide pH Sensors Using the Principle of Invariance," *International Journal of Chemical Engineering*, vol. 2021, 2021.
[132] R. Rahimi *et al.*, "A low-cost flexible pH sensor array for wound assessment," *Sensors and Actuators, B: Chemical*, vol. 229, pp. 609–617, 2016.
[133] Y. Laffitte and B. L. Gray, "Real-Time potentiometric pH-sensor using a screen-printable polyaniline composite on textiles," *FLEPS 2021 - IEEE International Conference on Flexible and Printable Sensors and Systems*, pp. 7–10, 2021.
[134] B. Lakard, G. Herlem, S. Lakard, R. Guyetant, and B. Fahys, "Potentiometric pH sensors based on electrodeposited polymers," *Polymer*, vol. 46, no. 26, pp. 12233–12239, 2005.

APPENDIX

Table 4 - Conversion Table of the Laser speed and power percentages to standard units.

Power (%)	Power (W)	Speed (%)	Scanning Speed (cms^{-1})
1	0.5	1	1.27
2	1.0	2	2.54
3	1.5	3	3.81
4	2.0	4	5.08
5	2.5	5	6.35
6	3.0	6	7.62
7	3.5	7	8.89
8	4.0	8	10.16

Table 5 - Sheet Resistance of one pass of graphene on paper with sodium tetraborate treatment

Power	Speed	Average (Ω/sq)	RSD
3	3	27,83	12%
3	4	65,95	4%
4	4	57,58	10%
4	5	46,44	14%
4	6	46,00	38%
5	6	58,98	5%
5	7	38,49	18%
5	8	38,85	33%
6	7	94,02	10%
6	8	57,94	16%

Table 6 - Sheet Resistance of one passes of graphene on waxed paper with sodium tetraborate treatment

Power	Speed	Average (Ω/sq)	RSD
5	5	44.05	44%
5	7	54.83	7%
6	6	26.20	42%
6	7	33.50	12%
6	8	39.23	20%
7	8	40.64	15%

Table 7 - Sheet Resistance of two passes of graphene on waxed paper with sodium tetraborate treatment

Power	Speed	Average (Ω/sq)	RSD
5	5	32,17	17%
5	7	24,90	5%
6	7	23,67	69%
6	8	16,18	13%
6	9	117,87	13%

Certificate of the CONGENTO Theory Course in Laboratory Animal Science

congento

CONGENTO LAS Theory Course for Functions A, C & D

According to the EC EWG Common Framework for Education and Training in Laboratory Animal Science[1]

We hereby certify that,

Cristina Alejandra Paublini Ornelas

successfully completed the CONGENTO Theory Course in Laboratory Animal Science, designed to fulfil the requirements of Directive 2010/63 for people working with **Rodents** (mouse and rat), on May 16th 2022.

Core Modules - Functions A, B, C & D

- 1- National legislation
- 2- Ethics, animal welfare and the Three Rs (level 1)
- 3.1- Basic and appropriate biology – species specific (theory)
- 4- Animal care, health and management – species specific (theory)
- 5- Recognition of pain, suffering and distress - species specific
- 6.1- Humane methods of killing (theory)

Function-specific Modules - Function A

- 7- Minimally invasive procedures without anaesthesia – species specific (theory)

Function-specific Modules - Function C (Additional)

- Module 23 - Advanced animal husbandry, care and enrichment practices

Dolores Bonaparte, DVM
Course Design and Coordination

Sofia Leocádio
Course Administration

(1) http://ec.europa.eu/environment/chemicals/lab_animals/pdf/Endorsed_E-T.pdf

Co-financed by: FCT Lisb@20[20] PORTUGAL 2020

CONGENTO LAS Theory Course for Functions A, C & D

According to the EC EWG Common Framework for Education and Training in Laboratory Animal Science [1]

COURSE CONTENTS

Co-financed by: FCT Lisb@20[20] PORTUGAL 2020

	SESSIONS	1 National legislation	2 Ethics, animal welfare and the Three	3.1 Basic and appropriate biology –	4 Animal care, health and management –	5 Recognition of pain, suffering and distress -	6.1 Humane methods of killing (theory)	7 Minimally invasive procedures without	23 Advanced animal husbandry, care and
CORE MODULES	C1- Science vs. Ethics	X	X						
	C2-Welfare and 3R	X	X			X			
	C3-Legislation	X							
	C4-Severity + Humane endpoints	X	X		X	X			
	C5-Clinical evaluation				X	X			
	C6-Harm-benefit evaluation	X	X		X	X			
	C7-Genetic standardisation		X	X	X				X
	C8-Genetically altered models			X					X
	C9-Working with GA animals		X		X	X			X
	C10-Microbiological standardisation			X	X				
	C11-Health, Safety and Animal Use				X				
	C12- Introduction to Feeding & Nutrition			X	X				
	C13-Introd. to admin & sampling procedures			X				X	
	C14-Euthanasia			X			X		
	C15-Public Outreach		X						
RODENT MODULES	R1-Rodent biology			X					
	R2-Behaviour + welfare		X	X		X			
	R3-Rodent Facilities				X				X
	R4-Rodent Housing Systems				X				X
	R5-Rodent husbandry				X				X
	R6-Rodent Feeding & nutrition				X				X
	R7-Rodent Reproduction			X	X				X
	R8-Rodent Colony Management			X	X				X
	R9-Rodent transport & acclimatization				X				X
	R10-Recog pain, suffering & distress				X	X			
	R11-Rodent Disease Management				X	X			X

(1) http://ec.europa.eu/environment/chemicals/lab_animals/pdf/Endorsed_E-T.pdf

Certificate of the IGC's Practical Course on Laboratory Animal Science in Mouse

GULBENKIAN SCIENCE

congento

IGC's Practical Course on Laboratory Animal Science in Mouse and Zebrafish

Certificate

We hereby certify that **Cristina Alejandra Paublini Ornelas**

successfully completed the IGC's Practical Course on Laboratory Animal Science in Mouse, held on May 25th 2022 at the Instituto Gulbenkian de Ciência, Oeiras. This course followed the EU recommendations for Functions A + D in Laboratory Animal Science.

Manuel Rebelo, PhD
Model Organism Facility Head, IGC

Ana Sofia Leocádio, BSc
Mouse Facility Specialized Technician, IGC

Joana Bom, MSc
Mouse Facility Manager, IGC

This practical course covered the following topics:

Function Specific Modules – Function A
3.2 – Basic and appropriate biology – species specific (practical)
7 – Minimally invasive procedures without anesthesia – species specific (theory)
8 – Minimally invasive procedures without anesthesia – species specific (skills)

Function Specific Module – Function D
6.2 – Humane methods of killing (skills)

Plenary sessions:
- Introduction to the Course and Legal aspects
- Introduction to Anesthesia in Mice

Hands on sessions:
- Mice Husbandry and Case Studies
- Handling and Restraint of Mice (manual and mechanical restrainers)
- Identification methods in Mice (scissors, ear punch, temporary marking)
- Administration of substances in Mice via intraperitoneal, subcutaneous, intradermal, intravenous and oral gavage
- Sampling techniques in Mice: blood collection from facial vein, submental vein and cardiac puncture; feces and urine collection
- Euthanasia in Mice: cervical dislocation

Additionally, Core Modules were covered in the SPCAL theoretical course

Core Modules
1 – National legislation
2 – Ethics, animal welfare and the Three Rs (level 1)
3.1 – Basic and appropriate biology – species specific (theory)
4 – Animal care, health and management – species specific (theory)
5 – Recognition of pain, suffering and distress – species specific
6.1 – Humane methods of killing (theory)